Novel approaches for direct exoplanet imaging: Theory, simulations and experiments

Por, E.H.

Chapter 1

Introduction

> *"It is as unlikely that a single world should arise in the infinite as that one single ear of corn should grow on a large plain."*
> – Metrodorus of Chios, fourth century BC

The question of the existence of life outside of Earth has long fascinated humanity. The ancient Greeks, notably Democritus and Epicurus, entertained the idea of cosmic plurality, the existence other life-bearing "worlds". The term "world" here refers more to the modern-day notion of parallel universes than that of other planetary systems. With the strong opposition of Plato and Aristotle, who argued for a perfect, unique and stationary world, the debate was largely decided against cosmic plurality in the Western world.

This stance was challenged in the Renaissance after Nicolaus Copernicus proposed the heliocentric model. This discovery demonstrated that the Earth was not the center of the universe and that the planets were not that much different from Earth. This led to the hypothesis that these other celestial bodies could be inhabited. In fact, there were two possibilities: either the Earth was somehow unique, a hypothesis that evolved into the modern-day *Rare Earth hypothesis*, or that life was common and that every other planet was inhabited. Nowadays it may be considered amusing that Sir William Herschel was a proponent of the latter theory, arguing that, even though the Moon seemed to have little to no atmosphere and no large seas on its surface, *"we can certainly not object to the conveniences afforded by the moon, if those that are to inhabit its regions are fitted to their conditions, as well as we on this globe are to ours"* and that *"I believe the analogies that have been mentioned are fully sufficient to establish the high probability of the moon's being inhabited like the earth"*.

While extra-solar planets, planets that orbit stars other than our own Sun, had long been hypothesised, the first discovery of an exoplanet puzzled scientists (Wolszczan & Frail, 1992). The two exoplanets orbit a pulsar, the rapidly rotating collapsed core of a giant star after a supernova. At the time, there was no known pathway for planets to survive a supernova. A third object orbiting the same pulsar was found two years later (Wolszczan, 1994). Only a few other *pulsar planets* have been found since (Rodin, 2019; Suleymanova & Rodin, 2014).

Only three years after this first discovery, an exoplanet was found around a Sun-like star (Mayor & Queloz, 1995). The mass of this planet, 51 Pegasi b, is about half of that of Jupiter, and it orbits its star in just over four days, making it about seven times closer to its host star than Mercury to the Sun. This small orbital distance makes the planets temperature a scorching 1000 °C. Additionally, the planet is likely *tidally locked* with its star, a phenomenon that makes one side of the planet always face its host star, similar to how the Moon always shows the same hemisphere to Earth. At that time, there was no known formation process that could produce such a massive planet that close to its host star. Since this discovery, many other exoplanets like 51 Pegasi b have been found, proving that they are quite common (e.g. see Fischer et al., 2016, for a review). This class of exoplanet is now collectively known as *hot Jupiters*.

Having demonstrated that finding exoplanets was possible with the technology at the time, astronomers embarked on a journey to find more. In the last two decades we have found out that most stellar systems contain multiple exoplanets, and on average every system has one planet orbiting in the habitable zone, where water can be liquid on the planet's surface (Dawson & Johnson, 2018a; Udry & Santos, 2007; Winn & Fabrycky, 2015). Most striking is the diversity of discovered planets. We have seen super-Earths, planets that have masses a few times that of our Earth composed of iron and silicates. We have seen sub-Neptunes, planets that have radii smaller than Neptune yet more massive (Luque et al., 2019). We have seen super-puff planets, which have radii larger than Neptune yet weigh only a few times the mass of our Earth (Libby-Roberts et al., 2020), though these might actually be smaller planets with giant ring systems that make them appear larger than they actually are (Piro & Vissapragada, 2020). We even have seen planets that seem to be disintegrating or evaporating, shedding large amounts of dust in their wake (Rappaport et al., 2012; van Lieshout et al., 2016).

The topic of this thesis is focused on the technology behind these discoveries, in particular for the method of *direct imaging*. This method attempts to image the exoplanet directly rather than infer its existence indirectly. This has the advantage of enabling spectroscopic characterization of the planets atmosphere, allowing us to infer its chemical composition and search for biomarkers, features that indicate the presence of extraterrestrial life on its surface. Direct imaging requires extensive technical knowledge of the behaviour of light, complex dynamic optical systems to mold it, and advanced computational tools to design and operate this optical system,

and to analyze the data produced by it.

In this introductory chapter, I give a brief outline of our current understanding the formation of planetary systems, then lead into the techniques using for detecting exoplanets. Of particular importance to this thesis is *direct imaging*, which deserves a more lengthy introduction. I conclude with an outline of how I contributed to the techniques used in direct imaging, what future directions are likely to progress this field and answer our current questions for exoplanet formation.

1.1 Star and planet formation

Star and planet formation is a complex process that covers a wide range of length and time scales. As star formation is inherently linked to planet formation, I will first discuss star formation before transitioning to planet formation. Figure 1.1 shows schematically an overview of the different stages of the entire process.

1.1.1 From molecular cloud to young stellar system

Molecular clouds consist of mostly hydrogen, helium, carbon monoxide, nitrogen gas and small silicate dust particles. Due to small density fluctuations, these clouds will become gravitationally unstable and contract into multiple cores, each with a mass of a few solar masses. These cores will slowly collapse, and form into proto-stars (Shu, 1977). Because of conservation of angular momentum, the rotation of the core will gradually speed up during its collapse. Small random motions cause a deviation from a perfect spherical collapse, resulting in a non-zero amount of angular momentum within the cloud. The cloud collapses and as the gas kinematically redistributes the momentum within the cloud, a preferred rotational axis is defined, forming a flattened disk structure. The pseudodisk will gradually flatten out and turn into a *proto-planetary disk*, mostly supported by the rotation of the disk (Bate, 1998; Matsumoto & Hanawa, 2003).

At this point, the star accretes most of its mass via the disk, with viscosity being the main driver for accretion (Shakura & Sunyaev, 1973). However, the disk is replenished faster from the core envelope, leading to the disk growing in mass. If the disk is heavy enough, it may itself become gravitationally unstable, and start to form spiral density waves and clumps (Kratter & Lodato, 2016). When the envelope runs out of material, the disk will start to deplete its gas, which is either accreted by the protostar or driven away by energetic processes such as stellar winds, photoevaporation

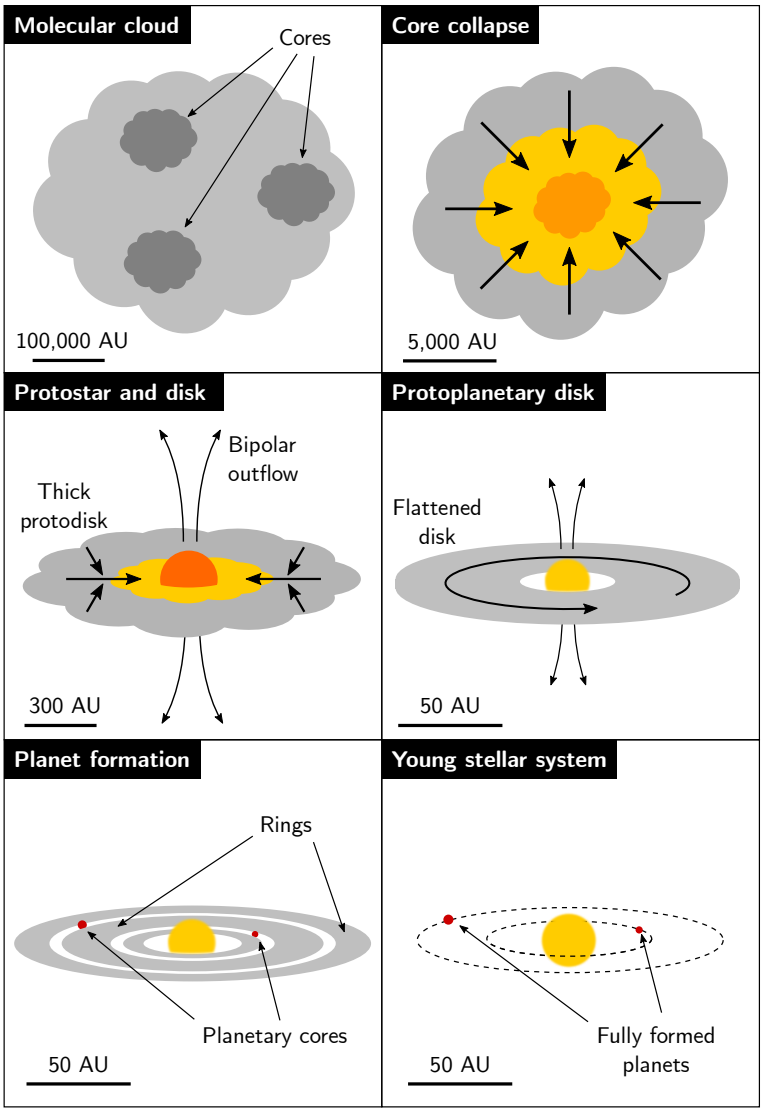

Figure 1.1: A schematic overview of the stages of star and planet formation, from a molecular cloud to a young stellar system. The scales indicate typical length scales for that stage.

or tidal encounters (Hollenbach et al., 2000). When all gas is depleted, the proto-planetary disk has turned into a *debris disk*. This transition from proto-planetary disk to debris disk takes a few million to ten million years and as there is no gas anymore after the disk becomes a debris disk, at least all giant planets must be formed during the proto-planetary disk stage.

1.1.2 Pathways for planet formation

One pathway of planet formation is gravitational instability within the proto-planetary disk. Especially in the outer regions of the disk, where collapse is easier, clumps may start to contract to form giant proto-planets (Boss, 1997). These grow by accreting gas until its orbit is cleared out. Their composition will be the same as the disk out of which they are born, and will therefore be close to that of the star. These giant planets may migrate through the disk (Paardekooper & Mellema, 2006), and provide a possible explanation for hot Jupiters (see also the review by Dawson & Johnson, 2018b).

Rocky exoplanets are formed via another pathway called core accretion. In the protoplanetary disk, small dust grains stick together if they hit each other (Dominik et al., 2007). Once the grains become heavy enough, they decouple from the gas and settle in the midplane of the disk in a process called *vertical settling*. This concentrates grains and promotes further grain growth. As the gas in the disk is partially supported by its pressure gradient, it rotates slightly slower than the local Keplerian velocity. The decoupled grains however do not feel this pressure gradient and orbit at Keplerian velocity. They feel a slight headwind which slows them down and causes them to drift radially inward and spiral towards the star. When particle sizes become on the order of a few millimeters, we start to call them *pebbles*. When pebbles collide, they tend to fragment instead of stick together, and pebbles will therefore not grow to larger sizes (Windmark et al., 2012). Additionally, pebbles will drift too quickly towards the star to aggregate into larger particles that are less susceptible to the radial drift. This problem is known as the *meter size barrier*.

Several mechanisms have been proposed to overcome this barrier, all of which try to concentrate the pebbles to promote growth. For example, if there is a gap in the disk, pebbles will accumulate at the outer edge of the gap as there is no headwind in the gap itself. Another possibility are *streaming instabilities*, where the interaction between the stream of solids and gas in the disk produce dense filaments which can provide densities of over 1000 times the local gas density (Johansen et al., 2011, 2015). Finally, *snowlines*

can create local pressure bumps which trap pebbles. Frozen ice particles drift radially inward and start sublimating when they get hot enough. The resulting gas does not drift inwards, leading to local enrichment of the gas with that element (Ciesla & Cuzzi, 2006; Öberg et al., 2011). Furthermore, the ices on the pebbles may make them stickier outside the iceline, which can further promote the grain growth rate. If these planetesimals become heavier than about ten Earth-masses, they start to accrete the gas and dust in their orbit and finally become a gaseous giant planet (Ikoma et al., 2000). Lower-mass planetesimals may never accrete any gas and become rocky exoplanets. Both of these types of planets may migrate through the disk.

1.1.3 Atmospheric composition and biomarkers

As the accreted gas has a different chemical composition as function of the distance from the star, we can probe the birth site, method of formation and migration history of an exoplanet by looking at this composition. Spectroscopy of exoplanets can tell us this composition, and also about the existence of life on these exoplanets through the detection of *biomarkers* (Schwieterman et al., 2018). Life (as we know it) produces disequilibrium chemistry in an exoplanet atmosphere (Krissansen-Totton et al., 2016), for example molecular oxygen as the byproduct of photosynthesis. Oxygen can be observed either directly with the A-band at $\sim$ 760nm, or indirectly by looking for ozone, which is created in the upper stratosphere when oxygen is exposed to ultra-violet light. Another biomarker is the vegetation red edge, the rapid change in reflectance of vegetation in the infrared resulting from the absorption spectrum of chlorophyll (Tucker, 1979). An interesting recent example is the detection of phosphine (PH_3) gas in the cloud deck of Venus with no currently known abiotic production routes (Greaves et al., 2020). Any single biomarker on their own could be the result natural processes, so we would require the detection of multiple separate biomarkers for an unambiguous statement of life on other planets.

1.2 Observational techniques for finding planets

Many techniques for detecting exoplanets have been developed in the last few decades. Figure 1.2 shows all discovered exoplanets coloured by their primary detection technique. For planets with unknown mass, its mass was estimated from their radius using the mass-radius relations in Bashi et al. (2017). Clearly, each technique has its own biases and strengths, making

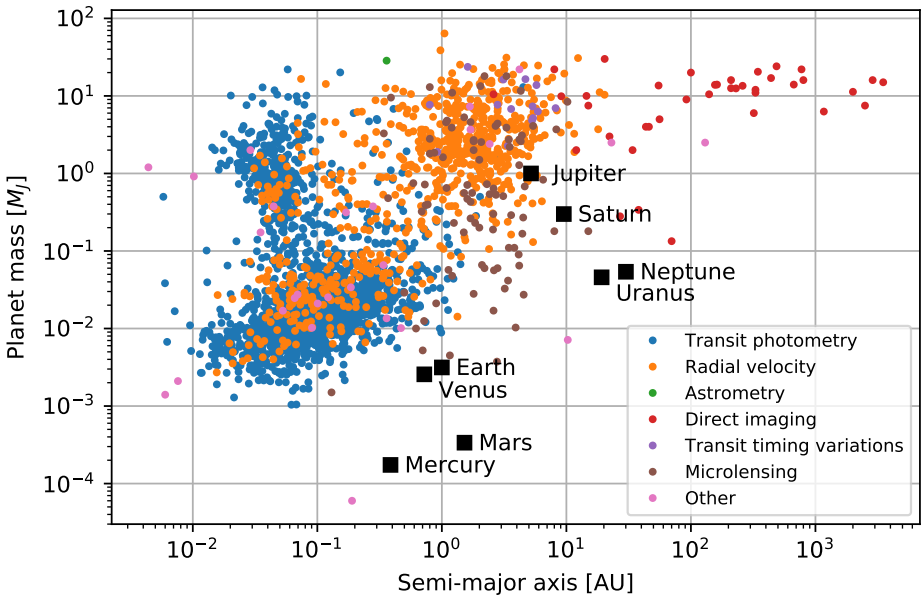

Figure 1.2: The mass and semi-major axis of all discovered exoplanets as of August 2020, coloured by their discovery method. Planets in our solar system are also shown for comparison. Data is taken from the NASA Exoplanet Archive.[1]

them more sensitive in different parts of the parameter space. Therefore, it is necessary to use multiple techniques simultaneously to obtain a more unbiased and complete view of exoplanets. It is outside of the scope of this introduction to discuss all methods in detail; I will briefly discuss the four main methods shown in Figure 1.3.

1.2.1 Transit photometry

Transit photometry has been the most prolific detection method over the years, especially with the launch of the dedicated survey telescope Kepler (Borucki et al., 2010). This method looks for the characteristic periodic dimming which occurs as the planet passes in front of their host star. During the transit, the amount of light received will be reduced proportional to

[1]The NASA Exoplanet Archive is operated by the California Institute of Technology, under contract with the National Aeronautics and Space Administration under the Exoplanet Exploration Program (`https://exoplanetarchive.ipac.caltech.edu/`).

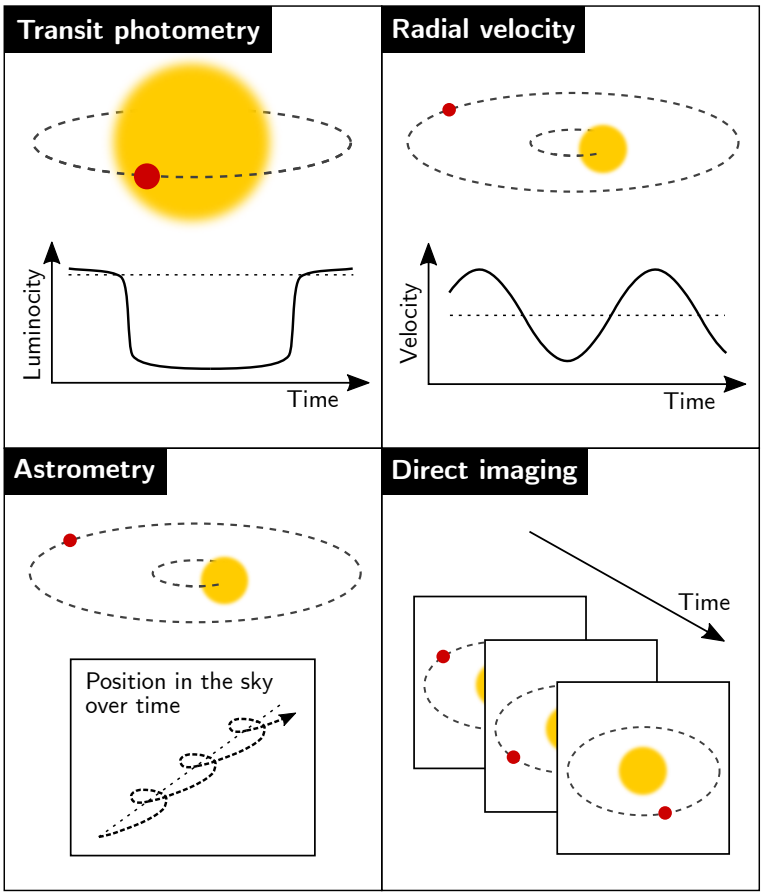

Figure 1.3: Four of the main exoplanet detection methods: transit photometry, radial velocity, astrometry and direct imaging.

the ratio of the areas of the planet and star. Transit depths can vary with Jupiter-sized planets producing a $\sim 1\%$ and Earth-sized planets a $\sim 0.1\%$ drop in flux. Additionally, spectroscopy during the transit can provide us with information on the atmospheric composition as light passing through the atmosphere is partially transmitted depending on wavelength, making the planet appear slightly larger or smaller at different wavelengths. Transits however relies on the fortunate alignment of the planet and star with respect to our point of view. Close-in planets have a higher chance of transiting, with hot Jupiters having a $\sim 10\%$ and Earth-analogues a mere $\sim 0.5\%$. Furthermore, we are biased towards small-period planets as these produce more transits in a given time interval, making it easier to extract

their signal from background noise. Larger planets produce a larger transit depth and are therefore easier to detect as well. This makes transits especially sensitive for hot Jupiters and super-Earths. Over 3000 transiting planets have been detected by *Kepler* alone, and its success has inspired several more satellites, notably TESS (Ricker et al., 2014), PLATO (Rauer et al., 2014) and CHEOPS (Rando et al., 2018).

1.2.2 Radial velocity

The *radial velocity* method is often used in conjunction with the transit method. Radial velocity looks for the small periodic reflex motion of the star when a planet is orbiting it. The size of the reflex motion is directly proportional to the mass of the planet, making heavier planets easier to detect. Typical reflex motions are $\sim$ 30 m/s for a hot Jupiter and $\sim$ 3 cm/s for an Earth-analogue. Radial velocity measures the mass of the planet, or more precisely, a lower bound of the mass in the form of the mass function $M_p \sin i$: if the orbit is inclined only part of the reflex motion will be seen. In case a planet is seen both with the transit and radial velocity method, we know the inclination as the orbit must be close to edge-on to be able to transit, and we can derive an estimate for the bulk density of the planet. Similarly to the transit method, there is a bias for small-period exoplanets as the multiple orbits can be stacked to decrease the noise over a given observation period. Detection is often limited by calibration of the spectrograph or astrophysical noise caused by stellar activity, which makes radial velocity worse for young stars.

1.2.3 Astrometry

Astrometry has so far produced fewer planet detections than the transit and radial velocity methods, but this is set to change with the GAIA mission (Gaia Collaboration et al., 2016). Astrometry looks at the reflex motion of the star as a planet is orbiting it by accurately measuring the centroid of the star's image with respect to a fixed reference frame. Astrometry is biased towards close-in planets where the orbital period of the planet is about twice the duration of the GAIA mission (Sahlmann et al., 2016, 2018). It can detect planets at any orbital inclination, removing one significant bias from the other two earlier methods, is far less limited by astrophysical noise and can be applied stars over a wide range of stellar ages. The GAIA mission will discover and measure several thousands of giant planets out to 3-4 AUs from stars within 200 pc at the end of the full mission (Casertano et al.,

2008) and will discover on the order of 10 planets around nearby bright stars suitable for observation with the Roman Space Telescope (Beichman et al., 2018).

1.2.4 Direct imaging

Direct imaging attempts to take an image of the exoplanet spatially separated from its host star. Direct imaging looks directly at the light of the planet, unlike the indirect methods described above, and can take spectra of the light emerging from the exoplanet and its environs. The main challenge of direct imaging stems from the high contrast ratio between the light from the planet and that of the star. This contrast ratio is a strong function of the wavelength of the observations. At optical wavelengths we are looking at reflected light off of the planet, where this contrast ratio is typically $\sim 10^8$ for Jupiter-analogues and $\sim 10^{10}$ for Earth-analogues around a Solar type star. At infrared wavelengths, however, for younger planetary systems (ages less than 500 Myr or so) we instead see the thermal radiation from the planet, which is still cooling down from the formation process. This improves the contrast ratio to $\sim 10^5$ for Jupiter analogues. Additionally, the small angular separation between the planet and the star makes it difficult for an instrument to distinguish between stellar and planet light.

Figure 1.4 shows the contrast (in reflected light) and angular separation for all discovered exoplanets to date. The planet-to-star flux ratio is estimated from the planet radius and physical separation, and assumes that the planet is observed at quadrature. If the planet radius is not known, as is the case for most radial velocity planets, it is estimated from the planet mass analogous to Lovis et al. (2017). It is clear that observing exoplanets in reflected light is extremely challenging, requiring intricately designed instruments and advanced data processing techniques to produce high-quality data.

1.3 Anatomy of a high-contrast imaging instrument

Diffraction plays an integral role in high-contrast imaging. Even for a perfect optical system, diffraction provides the fundamental resolution of the images that we achieve. For an unobstructed circular telescope pupil, the smallest angular size $\Delta\theta$ that we can resolve is

$$\Delta\theta = 1.22\lambda/D, \tag{1.1}$$

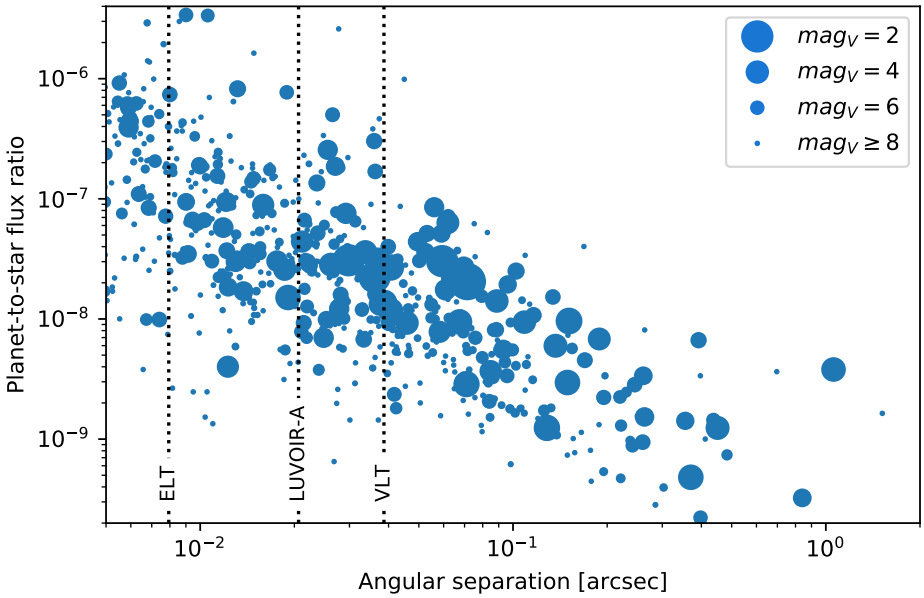

Figure 1.4: A contrast-separation plot for all discovered exoplanets as of August 2020 in the visible. The marker size indicates the magnitude of their host star in the optical (V-band). Approximate inner working angles are shown for the VLT, ELT and LUVOIR-A telescopes at $2\lambda/D$ for $\lambda = 750$nm. Data is taken from the NASA Exoplanet Archive.

where λ is the wavelength of the light and D is the diameter of the telescope mirror. Any object smaller than this size will look like the point spread function (PSF) of the telescope, which is fully determined by the shape of the telescope pupil, as seen in Figure 1.5 panel (a). Most stars are unresolved by current telescopes, and will therefore look like the telescope PSF. In Fig. 1.5, I show a few example of PSFs for various telescopes around the world. Generally, less than 80% of the star light will be contained within the central core of the PSF. The rest of the light is spread out into a large number of successively fainter *diffraction rings* around the core. This means that at the location of the planet, typically only a few to a few tens of diffraction widths away from the star, most of the received photons originate from the diffraction halo of the star and not the planet, even when we observe with a idealized perfect optical system. In order to filter out this unwanted light and reveal the dim planet buried underneath, we use a *coronagraph*. The coronagraph is an optical device – an angular filter –

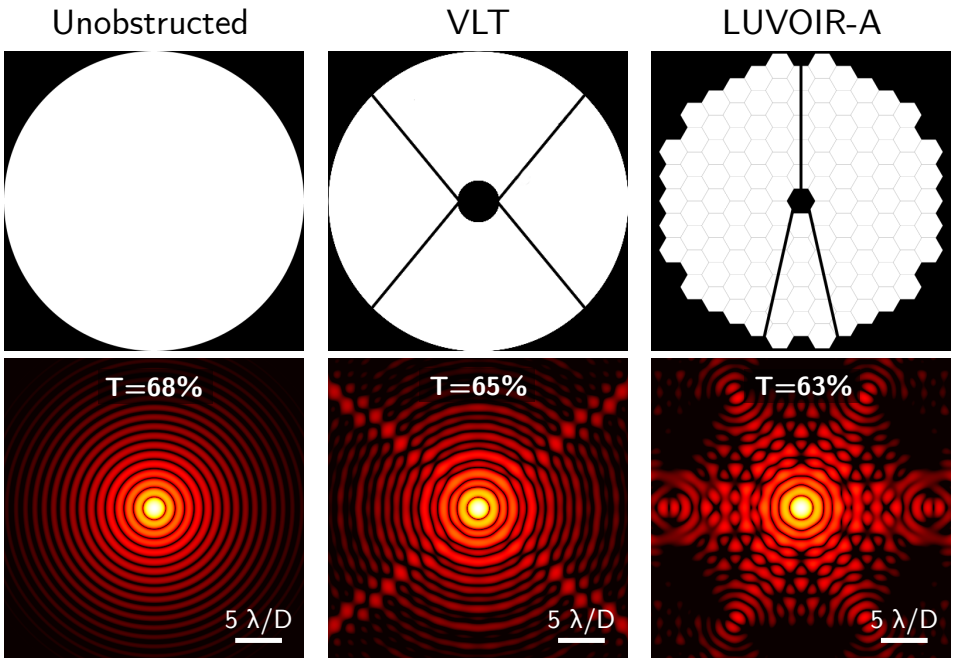

Figure 1.5: Simulated point spread functions for (a) an unobstructed circular pupil, (b) the VLT, and (c) the LUVOIR-A telescope. The throughput T is indicated on each of the PSFs and is calculated as the fraction of the power inside a $1.4\lambda/D$ circular aperture centered on the peak.

that is able to suppress the on-axis star light, while letting through most of the off-axis light from planets, the disk, or background objects.

In a perfect world, a coronagraph by itself will always produce high quality coronagraphic images, in practice this is not the case. As starlight propagates through space, the originally spherical wavefronts centered on the star gradually become flatter, like ripples in a pond expanding out towards the edges. When the light wave arrives at Earth, its wavefront will be almost completely flat. However, when passing through the atmosphere, this flat wavefront becomes distorted as it propagates through the Earth's turbulent atmosphere. Changes in the temperature of the air create a time and position dependent index of refraction across the telescope pupil (Fried, 1966). Imperfections in the manufactured optics, or the alignment of these optics in our optical system, provide an additional source of wavefront distortion. Both these sources of wavefront errors are dynamic: atmospheric wavefront errors will change on on millisecond timescales as the moving tur-

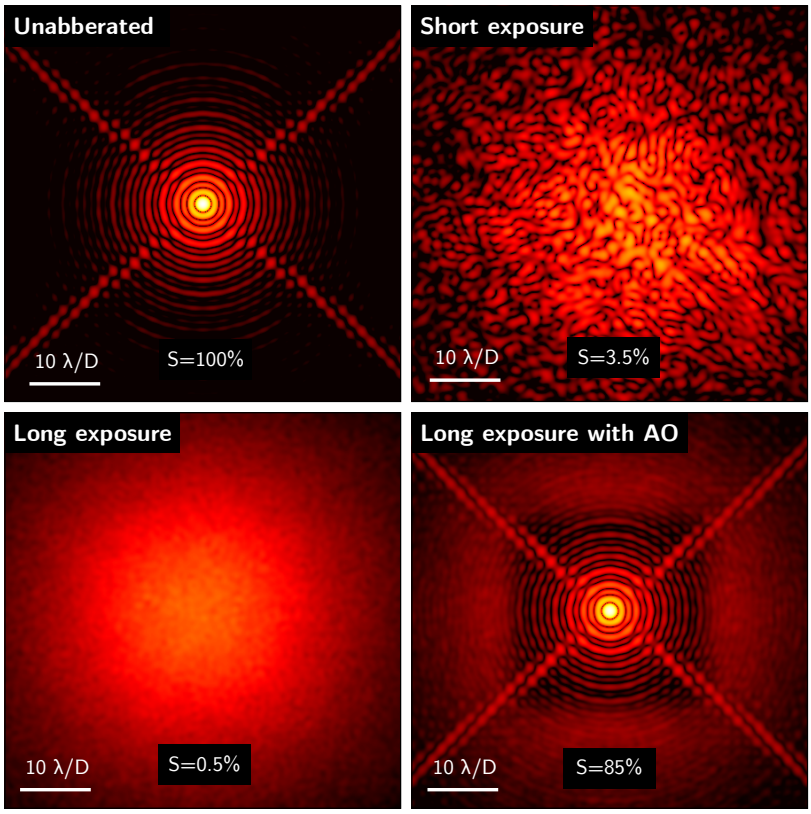

Figure 1.6: Simulated focal-plane images for the VLT in various circumstances. (a) No aberrations; (b) Short exposure with atmospheric aberrations; (c) Long exposure through atmospheric turbulence; (d) Long exposure through atmospheric turbulence with AO.

bulence in the atmosphere is blown across the telescope pupil (Greenwood, 1977) and the alignment of the optical train will change on minute to hour timescales, as the telescope moves to track the star across the sky over the course of the night (Hinkley et al., 2007; Martinez et al., 2013; Milli et al., 2016). Temperature fluctuations and gradients within the instrument may move optics due to thermal expansion of the mechanics to which the optics are mounted.

As our coronagraph is only designed to suppress light with a flat wavefront, it will transmit any deviations from this ideal wavefront, resulting in a cloud of speckles around the optical axis. If the wavefront aberrations are strong enough, typically more than 1/4 of a wave across the pupil, the

core of the PSF is also broken up, spreading the light over a larger area which makes it much more difficult to detect a planet. A rough metric for the wavefront quality is called the Strehl ratio S, which is approximated by $e^{-\sigma^2}$ where σ is the root mean square deviation of the wavefront phase in radians over the pupil. For an ideal optical system, $S = 1$ and for most ground based high contrast imaging cameras, $S \sim 0.6-0.9$ for 8 metre class telescopes at wavelengths of $1-3$ microns. We use *wavefront control system*, also called *adaptive optics* (AO) system for ground-based observatories, to reflatten the wavefront before the light passes into the coronagraph. This system measures the wavefront aberration and attempts to apply the opposite and equal aberration with a wavefront modulator. Figure 1.6 shows typical examples of focal-plane images for the VLT pupil with and without AO system.

Finally, we need to capture the planet light on a camera. This is the job of the *science instrument*. This part of the instrument provides both scientific data for the astronomer and calibration data for the coronagraph or wavefront control system. The calibration data allows us to further correct the scientific images for errors made by the coronagraph, the wavefront control system or any other optics in our instrument. In general, the science instrument can be simply a detector or a more complicated optical system, detecting the spectrum of light at each pixel with an integral field spectrograph, eg. SPHERE/IFS (Claudi et al., 2008) or GPI/IFS (Larkin et al., 2014), or detecting the polarization state at each pixel with a polarization beam splitter, eg. SPHERE/ZIMPOL (de Boer et al., 2020; Schmid et al., 2018), or both (Rodenhuis et al., 2014; Tinyanont et al., 2019).

1.3.1 The coronagraph

Many different types of coronagraphs have been developed over the last two decades. A comprehensive review of the current field of coronagraphy are in the excellent review articles of Guyon et al. (2006), Mawet et al. (2012) and Ruane et al. (2018). The focus of this section is to provide an overview of the considerations that need to be taken into account when designing a coronagraph, and the theory behind how a typical coronagraph suppresses star light.

End-to-end simulations

Any specific coronagraph design will be a compromise between a large number of different metrics. The environment that the coronagraph will be op-

erating in determines to what degree each of these metrics count towards the performance of the overall system. This makes it difficult to tell in advance which type of coronagraph will perform best in a specific system, and often extensive end-to-end simulations or even on-sky testing of actual implementations are required to reach a conclusion.

An example of the output of current state-of-the-art end-to-end simulations can be found in Figure 1.7 as performed for the proposed LUVOIR-A mission by AYO, the Altruistic Yield Optimizer (Stark et al., 2014; The LUVOIR Team, 2019). AYO operates in a simulated universe complete with simulated stars. A hypothetical mission is defined with coronagraph models, limited mission lifetime and estimated operating costs, and then attempts to detect and characterize exoplanets around these stars. AYO decides which stars too look at, for how long and with which coronagraph or observing mode, in order to maximize the exoplanet candidate yield and the number of characterized exoplanets at the end of the mission. Several simulated missions are usually performed to average out statistical errors and provide confidence intervals.

Figure 1.7 shows preliminary results for two different mission configurations, the first being the baseline LUVOIR-A mission and the second where one of the coronagraphs was replaced by a phase-apodized-pupil Lyot coronagraph (PAPLC), developed in Chapter 7 and 8 of this thesis. This shows that the PAPLC provides $\sim 25\%$ more exoplanet candidates, a significant improvement.

Terminology and design metrics

While we would prefer to perform complete end-to-end simulations to guide the design process, in most cases we do not have the time or the resources. Often the design is chosen subjectively by the coronagraph designer based on a number of simpler metrics. In this section, I give an overview of the definition of these metrics and in what way they impact the exoplanet candidate yield.

- One of the most obvious metrics is *raw contrast*. This describes to what level the starlight is suppressed. The raw contrast is the amount of light within a given aperture (usually defined as a small multiple of the FWHM of the central core PSF) at a given angular separation from the central star, and normalised to the total enclosed flux within the same aperture centered on the star. External factors, such as the performance of the wavefront control system and the post-processing

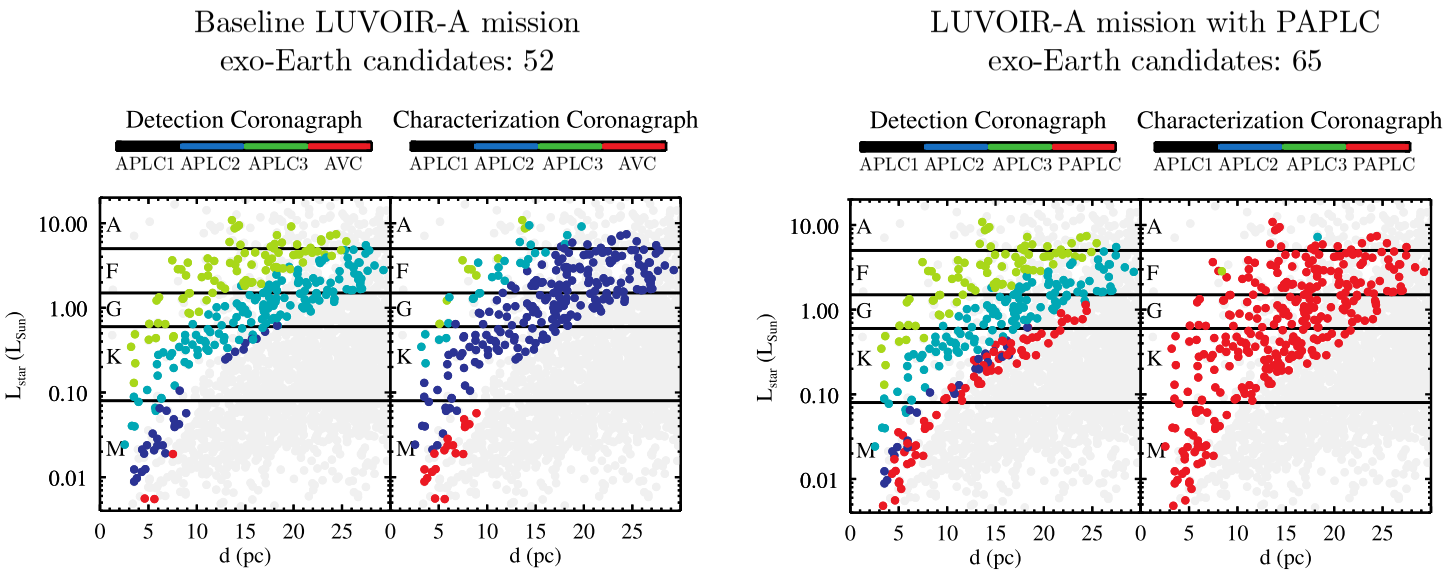

Figure 1.7: The luminosity-distance plots showing exo-Earth candidates for a simulated LUVOIR-A mission with the baseline coronagraph configuration (left) and a configuration where the apodized vortex coronagraph is replaced by the PAPLC (right). Simulations were performed by Chris Stark using the PAPLC design presented in Chapter 7. The PAPLC is chosen by AYO for almost all characterization observations.

techniques, may play a role in defining this quantity. Designing a coronagraph with a raw contrast much deeper than the wavefront control system is able to provide will not improve the quality of our images. Typically, we require raw contrasts of 10^{-5} – 10^{-8} for Earth-based observatories, and 10^{-8} – 10^{-10} (where the telescope diameter is smaller and therefore the diffraction limit is larger) for space-based observatories.

- Another metric is *planet throughput*. This describes the fraction of light that we receive from an exoplanet compared to an observation without the coronagraph inserted into the optical train. The apparent magnitude of Earth-analogues are expected to be $\gtrsim 26$ mag, even for those orbiting our closest stars, so we do not want to unnecessarily block/remove too many precious photons for our science instrument. Simulations show that a planet throughput of $< 25\%$ is deemed insufficient for exoplanet imaging, and planet throughputs of $> 50\%$ are to be preferred.

- Planet throughput is rarely independent of the relative location of the planet with respect to the star. Planet throughput starts at zero for a zero angular separation, as it will be located at the same position as the star and its light will be indistinguishable from star light and therefore suppressed in the same way. For planets at larger nonzero angular separations, planet throughput rises up to a certain maximum theoretical throughput. A convenient quantity is the *inner working angle*, which defines the angular separation where the planet throughput is half of the maximum planet throughput for that coronagraph. Mimimizing inner working angles allows us to look closer to the star at the expense of other metrics.

- A related metric is *field of view*. Some coronagraphs only obtain the contrast in a certain part of the focal plane, the region of interest. When performing blind surveys, we do not know where or even if there is an exoplanet. Coronagraphs with a larger region of interest are able to search more efficiently for exoplanets compared to coronagraphs with a smaller region of interest. One interesting case here are coronagraphs with a region of interest on only one side of the star, rather than in an annulus surrounding the star.

- *Robustness against low-order aberrations* is a useful property of a coronagraph. Dynamic misalignment of optics tend to induce mostly

low-order aberrations. While the wavefront control system tries to correct these continuously, some portion remains and we view these as drifting low-order aberrations during the observation. When a coronagraph is robust against these, we can handle lower photon fluxes as we do not need to control the aberrations as tightly as we otherwise would. However, as the throughput at small angular separations is mostly determined by the throughput of low-order modes, especially the inner working angle is most affected when making a coronagraph more robust.

- Robustness against specifically tip-tilt aberrations plays a big role in the *robustness against stellar diameter*. Future telescopes are becoming so large that they are on the verge of resolving the stellar surface for nearby stars. Stellar angular diameters can be as large as $0.01 - 0.1\lambda/D$ for 8-meter class telescopes observing nearby stars at wavelengths of scientific interest. Coronagraphs must therefore be designed to suppress an extended rather than a point source. The problem of stellar diameters primarily affects space telescopes compared to ground-based telescopes due to their deeper raw contrast requirement.

- An often overlooked metric is the *optical complexity* of the coronagraph design. Coronagraphs with a more complicated optical layout are more susceptible to misalignment. The more complex an optical element is, the more costly it will be to manufacture and the higher the chance of manufacturing errors or damage. On the other hand, the more complex a coronagraph is, the higher the design freedom, making it have higher performance compared to simpler coronagraphs.

- Finally, an *integration with wavefront sensing* can be extremely useful to have. Coronagraphs with a built-in wavefront sensor can provide continuous wavefront telemetry to the wavefront control system. As the wavefront sensing occurs at the plane of the coronagraph, this eliminates most non-common-path aberrations while also allowing simultaneous wavefront control and coronagraphic imaging.

There is a complex interplay of trade offs between the most significant factors in optical and scientific design of a given instrument, and there are several more that might be added to this initital list, depending on the specific science case and the engineering constraints.

An idealized coronagraph

Before discussing physical coronagraph implementations, it is instructive to first look at an idealized or "perfect" coronagraph. While these perfect coronagraphs cannot be manufactured, they can serve as the fundamental limit for coronagraphy: they allow us to see the optimal performance of an idealized coronagraph with which to compare actual coronagraph designs against.

The perfect coronagraph was introduced by Cavarroc et al. (2006) and projects the incoming electric field on an unaberrated pupil-plane electric field that represents an ideal point source incident on the telescope optics. This projection is then subtracted from the incoming light, providing the output electric field. The second-order perfect coronagraph can be represented by the operator

$$\mathcal{P}^{(2)}\{\Psi\} = \Psi - \mathrm{proj}_{V_2}\{\Psi\}, \tag{1.2}$$

where proj_{V_2} denotes the projection operator onto the vector space $V_2 = \mathrm{span}\,(\Pi)$, and Π denotes an unaberrated pupil-plane electric field. Any coronagraph can be ultimately represented by an operator and this operator has to be linear as the light levels in a telescope are not strong enough to excite non-linear optical phenomena. The coronagraph in Equation 1.2 is "perfect" in the sense that it maximally retains all light that is not star light, while fully suppressing all starlight and still being a linear operator.

In Figure 1.8, I show the image of a point source through a second-order perfect coronagraph at different angular separations from the optical axis, along with the core throughput, i.e. the amount of light transmitted in a $1.4\lambda/D$ diameter circle centered on the point source. As expected, the coronagraph suppresses all light when the object is on-axis and has almost no effect when the object is far from the optical axis. However, even at extremely small angular separations a significant fraction of light is transmitted: the coronagraph is very sensitive to low-order aberrations.

We can describe this mathematically as follows. For a small tip-tilt aberration, the input electric field is

$$\Psi_{\mathrm{tiptilt}} = \Pi \exp(\alpha x) \tag{1.3}$$

$$= \Pi(1 + \alpha x + \mathcal{O}(\alpha^2)), \tag{1.4}$$

which yields for the light through the coronagraph

$$\mathcal{P}^{(2)}(\Psi_{\mathrm{tiptilt}}) = \alpha \cdot (x\Pi - \mathrm{proj}_{V_2}\{x\Pi\}) + \mathcal{O}(\alpha^2)), \tag{1.5}$$

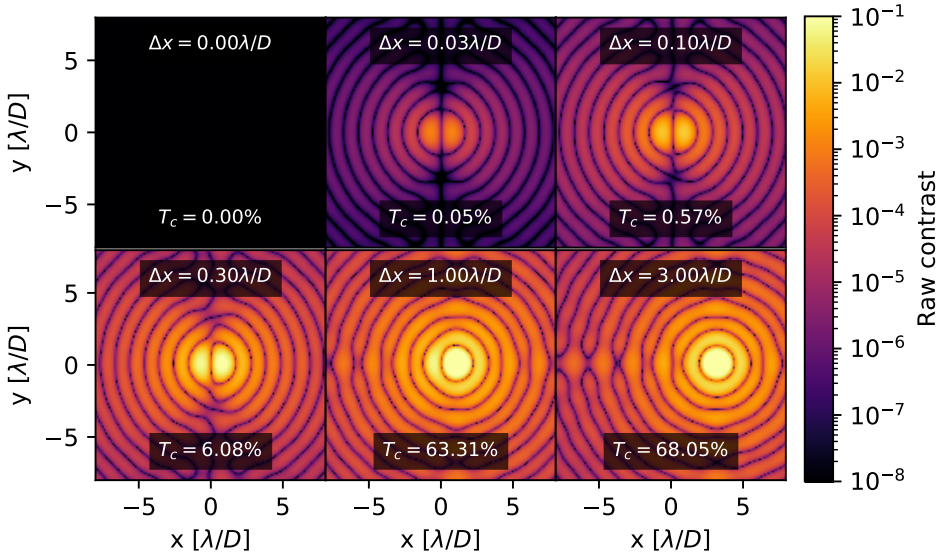

Figure 1.8: Images for on- and off-axis point sources through a second-order perfect coronagraph. For each image, the core throughput, the fraction of light inside a $1.4\lambda/D$ diameter circle centered on the object, is listed.

where x is the x-coordinate in the pupil. This shows a quadratic response in the intensity leaking through the coronagraph, $I_{\text{leak}} = |\mathcal{P}^{(2)}\{\Psi_{\text{tiptilt}}\}|^2 \propto \alpha^2$ as function of α, the strength of the aberration. This quadratic behaviour is the reason why this type of perfect coronagraph is known as a second-order perfect coronagraph.

Guyon et al. (2006) extends the perfect coronagraph to higher orders to add robustness to low-order aberrations. This is done by extending the vector space V_2 to include more than just the telescope pupil. For example, a fourth-order and sixth-order perfect coronagraph can be described by the vector spaces

$$V_4 = \text{span}\left(\Pi, x\ \Pi, y\ \Pi\right), \tag{1.6}$$

$$V_6 = \text{span}\left(\Pi, x\ \Pi, y\ \Pi, x^2\ \Pi, xy\ \Pi, y^2\ \Pi\right), \tag{1.7}$$

and the general n-th order perfect coronagraph as

$$\mathcal{P}^{(n)}\{\Psi\} = \Psi - \text{proj}_{V_n}\{\Psi\}. \tag{1.8}$$

Looking at the leakage light for a small tip aberration for a fourth-order

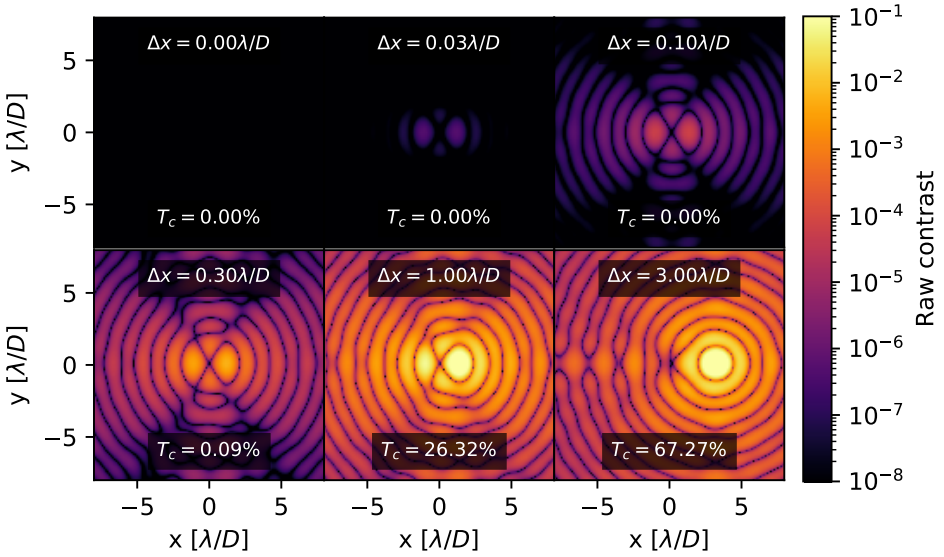

Figure 1.9: Images for on- and off-axis point sources through a fourth-order perfect coronagraph. For each image we list (i) the core throughput, and (ii) the fraction of light inside a $1.4\lambda/D$ diameter circle centered on the object. Compared to the same images for a second-order coronagraph, the amount of leakage light is strongly reduced, see Figure 1.8.

perfect coronagraph

$$\mathcal{P}^{(4)}(\Psi_{\text{tiptilt}}) = \alpha^2 \cdot (x^2\Pi - \text{proj}_{V_4}\{x^2\Pi\}), \tag{1.9}$$

we see a quartic response in intensity as function of α, the strength of the aberration. Likewise, for the sixth-order perfect coronagraph this yields a sixth-order polynomial response.

Looking at the same on- and off-axis images for the fourth-order perfect coronagraph in Figure 1.9, we can visually see this increased robustness to low-order aberrations. However, we can also see the increase in the inner working angle of the coronagraph. For close in planets, the incoming light contains predominantly low-order electric field modes which are now filtered out by the coronagraph and therefore do not count towards the planet throughput. Higher-order perfect coronagraphs have necessarily larger inner working angles.

The classical Lyot coronagraph

We now transition from the idealized perfect coronagraphs to physical implementations of coronagraphs. Physical coronagraphs typically consist of a series of pupil and focal planes, in each of which there may be a mask that modifies the complex electric field (i.e. both amplitude and phase of the wavefront). These masks are designed in such a way as to suppress the light from the star, while transmitting the light from the planet.

The first coronagraph was developed by Lyot (1939) and was originally intended for imaging the solar corona. It was later adapted for use with stars, and remains a standard layout for many coronagraphs. Its optical layout is shown schematically in Fig 1.10 along with the electric field in all relevant planes.

We will now trace the light through the Lyot coronagraph starting with the electric field just before plane A, $\Psi_{A-} = \Pi$. As there is no mask in this pupil plane, the light right after plane A is the same:

$$\Psi_{A,+} = \Psi_{A,-} \tag{1.10}$$
$$= \Pi. \tag{1.11}$$

Propagating to plane B, a focal plane, we get

$$\Psi_{B,-} = \mathcal{C}\{\Psi_{A,+}\} \tag{1.12}$$
$$= \mathcal{C}\{\Pi\}, \tag{1.13}$$

where $\mathcal{C}\{\cdot\}$ is a linear operator that propagates a field from the pupil to the focal plane, typically approximated with a Fraunhofer propagator. In this focal plane, we put a small opaque disk centered on the star. We call this mask $M(\mathbf{k})$. Just after this focal plane mask, the electric field is

$$\Psi_{B,+} = M(\mathbf{k}) \cdot \Psi_{B,-} \tag{1.14}$$
$$= M(\mathbf{k}) \cdot \mathcal{C}\{\Pi\}. \tag{1.15}$$

Note that this mask by itself only blocks the center of the field, and that outside this opaque mask nothing has changed. Bernhard Lyot realized that if we look at this field in the next pupil plane, plane C, most of the light is outside of the original telescope pupil. This can be seen in Fig. 1.10, but it is instructive to view this from a mathematical perspective as well. The electric field just in front of the Lyot stop mask is

$$\Psi_{C,-} = \mathcal{C}^{-1}\{\Psi_{B,+}\} \tag{1.16}$$
$$= \mathcal{C}^{-1}\{M(\mathbf{k}) \cdot \mathcal{C}\{\Pi\}\}, \tag{1.17}$$

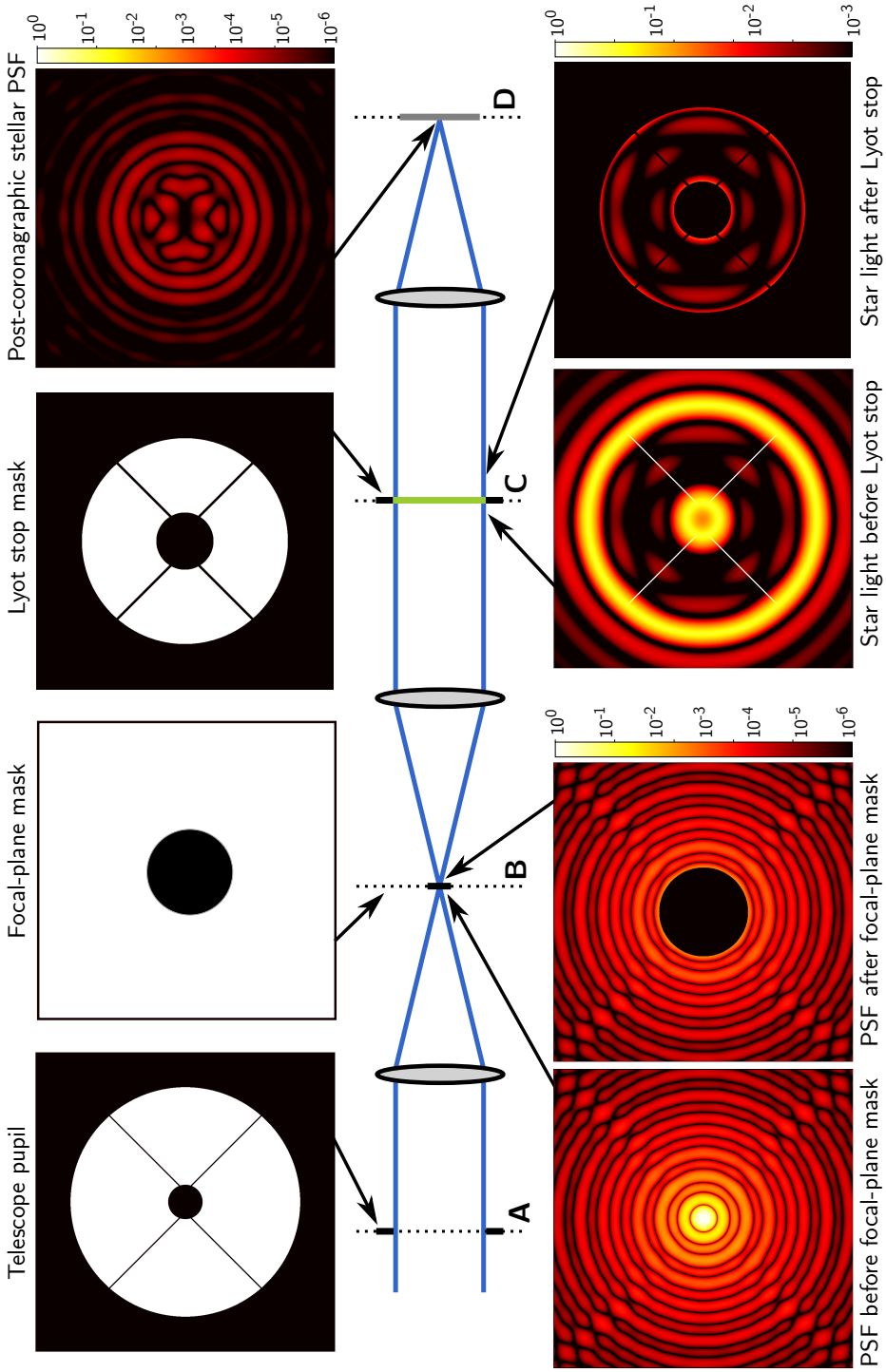

Figure 1.10: The propagation of light through a Lyot coronagraph.

which can be rewritten using Babinet's principle as

$$\Psi_{C,-} = \Pi - \mathcal{C}^{-1}\{(1 - M(\mathbf{k})) \cdot \mathcal{C}\{\Pi\}\}. \tag{1.18}$$

Comparing this to Eq. 1.2 for the perfect coronagraph, we can see a similar structure. Instead of subtracting a scaled version of the telescope pupil, we are subtracting a filtered version of the incoming field. As $(1 - M(\mathbf{k}))$ is a small circular aperture and the operator $\mathcal{C}\{\cdot\}$ is analogous to a Fourier transform, the second term is actually a low-pass-filtered version of the telescope pupil. Therefore the the subtraction will be good in the middle of the telescope pupil, but the hard edge of the telescope pupil is not well subtracted, yielding a bright ring on the edge of the pupil. The Lyot coronagraph blocks this starlight with a mask, nowadays called Lyot stop after its inventor Bernard Lyot. Planet light on the other hand will pass through mostly unhindered, as the majority of its light will be inside the telescope pupil.

Blocking with the Lyot stop mask $L(\mathbf{x})$ yields

$$\Psi_{C,+} = L \cdot \Psi_{C,-} \tag{1.19}$$

$$= L \cdot \left[\Pi - \mathcal{C}^{-1}\{(1 - M(\mathbf{k})) \cdot \mathcal{C}\{\Pi\}\}\right], \tag{1.20}$$

so that we can write the Lyot coronagraph operator $\mathcal{L}\{\cdot\}$ as

$$\mathcal{L}\{\Psi\} = L \cdot \left[\Psi - \mathcal{C}^{-1}\{(1 - M(\mathbf{k})) \cdot \mathcal{C}\{\Psi\}\}\right]. \tag{1.21}$$

While the Lyot coronagraph is very simple, it typically only suppresses the star by one or two decades in raw contrast. In fact, there is not enough design freedom to completely suppress the star while still having a reasonable planet throughput: no combination of focal-plane mask size and Lyot-stop diameter will make the two terms in Eq. 1.21 equal to each other. However, many modifications have been proposed to improve upon the traditional Lyot coronagraph.

Lyot-style coronagraphs with pupil-plane apodizers

The first of these was attempted as early as the late 1980's, where Ftaclas et al. (1988) notes that using a graded transmission mask in in the pupil plane before the focal-plane mask lets the Lyot stop suppress more light. We can see intuitively that by smoothing out any edges of the pupil makes it look closer to its low-pass-filtered version, which provides better stellar suppression. This technique was further developed by Soummer

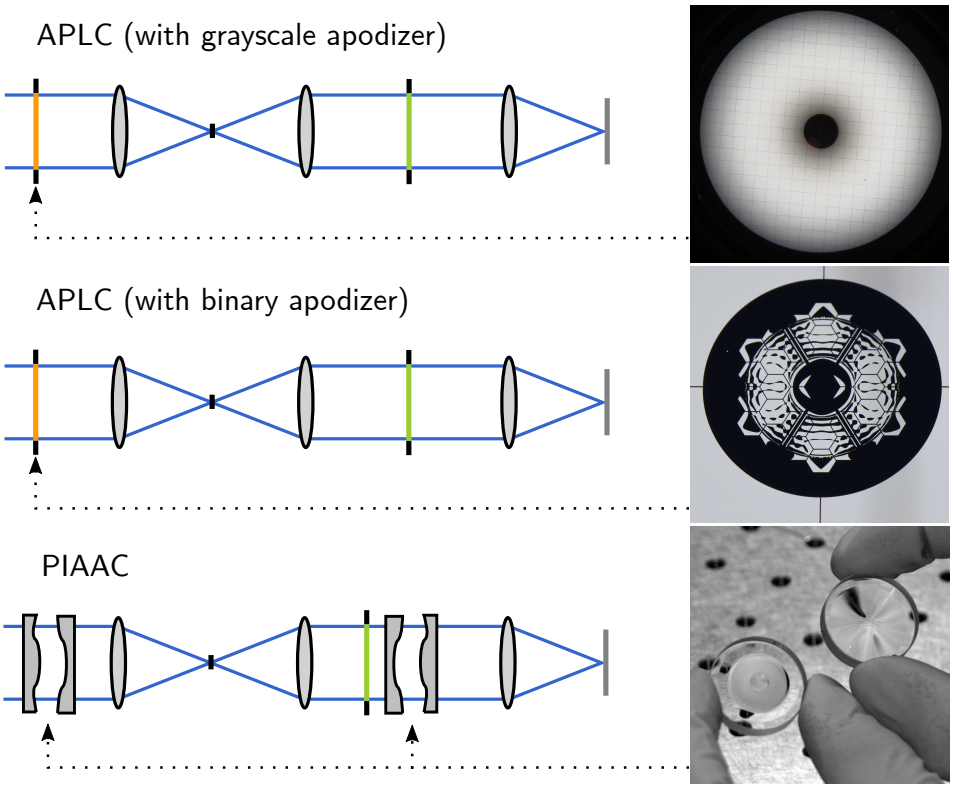

Figure 1.11: Schematic optical layouts of three types of Lyot coronagraphs with pupil-plane apodizers. The microscopy and photographic images are adapted from Sivaramakrishnan et al. (2010), Soummer et al. (2018), and Lozi et al. (2009).

et al. (2003a) and Soummer (2005), showing that a prolate apodization profile can fully suppress the star. Later on, the grayscale apodizers were replaced with binary masks as globally-optimal optimization methods were developed (N'Diaye et al., 2016; Zimmerman et al., 2016a). This collection of coronagraphs is now known as the apodized-pupil Lyot coronagraph (APLC) family. APLCs have seen widespread usage within the current generation of ground-based instruments, such as VLT/SPHERE (Guerri et al., 2011) and Gemini/GPI (Sivaramakrishnan et al., 2010). For a number of future space telescopes, the APLC is the baseline coronagraph, for example for the Roman Space Telescope (Zimmerman et al., 2016a) or the LUVOIR-A telescope (The LUVOIR Team, 2019; Zimmerman et al., 2016b).

Partially blocking light in the telescope pupil is wasteful: planet light passes through the apodizer mask in the same way as star light, so planet photons get absorbed as well, decreasing planet throughput. Guyon (2003) overcomes this problem by replacing the grayscale apodizer with two free form mirrors that redistribute the light in the pupil to achieve the same apodization as the apodizer mask would. This coronagraph is known as the phase-induced amplitude apodization (PIAA) coronagraph and yields more efficient coronagraphs as the apodization is achieved without any light loss. This comes at the cost of a higher optical complexity as freeform mirrors can be hard to manufacture with sufficient accuracy. Additionally, light at larger angular separations is significantly distorted by the pupil remapper, in some cases requiring the use of an inverse pupil remapper at the Lyot stop plane. This counteracts the distortion at the cost of further optical complexity.

Lyot-style coronagraphs with complex focal-plane masks

Another option that was explored was using a graded focal-plane mask (Kuchner & Traub, 2002). This type of coronagraph was later extended towards focal-plane masks that apodize both in amplitude and phase, forming the hybrid Lyot coronagraph (HLC) (Moody & Trauger, 2007), and has been chosen as one of the two coronagraphs on board of the Roman Space Telescope (Trauger et al., 2016). The focal-plane masks for the HLC are manufactured with metallic and dielectric layers deposited on a glass substrate (Trauger et al., 2016).

Roddier & Roddier (1997) proposes to replace the small opaque dot in the focal plane mask of the Lyot coronagraph by a small dot that induces a phase of π onto the light passing through. This corresponds to a mask transmissivity of -1 instead of 0, effectively subtracting twice the low-pass-filtered version from the original electric field. This allows for shrinking of the size of the focal-plane mask, making the phase-mask coronagraph more efficient at small angular separations.

The focal-plane mask is often manufactured using photolithographic techniques where the phase profile is etched directly into the substrate. This means that the applied phase shift will be dependent on the wavelength of the light, making the phase-mask coronagraph only capable of operating efficiently only close to its design wavelength. Soummer et al. (2003b) generalizes the phase-mask coronagraph by adding an additional ring around the central dot. This enables achromatization of the coronagraph, correcting for both size chromatism (the growth of the PSF as

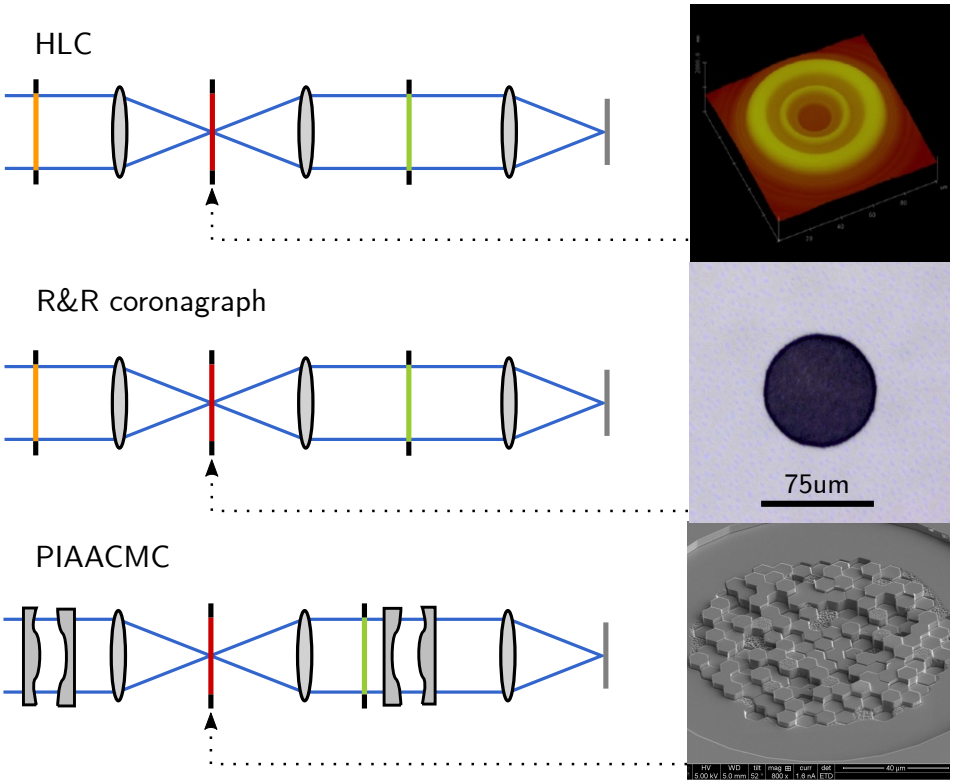

Figure 1.12: Schematic optical layouts of three types of Lyot coronagraphs with focal-plane apodizers. The scanning electron and optical microscope images are adapted from Trauger et al. (2016), Doelman et al. (2019), and Knight et al. (2018). While the image for the Rodier & Rodier (R&R) coronagraph depicts a microscopic image of a Zernike wavefront sensor focal-plane mask, the analogous image for the R&R coronagraph, although not manufactured, would look very similar.

function of wavelength), and phase chromatism (the chromatic response of the substrate material).

This phase-mask coronagraph can be combined with a pupil-plane apodizer (Soummer et al., 2003b) and the pupil remapper can be used to achieve higher throughput (Guyon et al., 2010). The focal-plane mask can be additionally divided into multiple zones to correct for chromatism, either in rings (Newman et al., 2016) or with hexagonal tiling (Knight et al., 2018).

Phase-mask coronagraphs

There are several types of coronagraphs that retain the optical layout of the Lyot coronagraph but use a different approach for the focal-plane mask. Rather than having a localized effect, their focal-plane masks extend out to infinity. The earliest example of these coronagraphs is the four-quadrant phase-mask (FQPM) coronagraph (Rouan et al., 2000). Its focal-plane mask consists of four equally-sized regions, alternating in phase between 0 and π and extending radially from the center. Higher-order versions have been developed as well, providing increased robustness against low-order aberrations (Murakami et al., 2008) in a similar fashion as higher-order perfect coronagraphs.

While these coronagraphs tend to have excellent planet throughput at large angular separations, the planet light is scattered when it hits the edges between neighbouring regions, so the planet throughput drops at those locations. This problem is solved by the vortex coronagraph, which replaces the discrete regions with a smoothly varying azimuthal phase gradient (Foo et al., 2005; Mawet et al., 2005). The number of times the phase hits 0 is known as the charge of the vortex, which acts in a similar way to the order in perfect coronagraphs (Ruane et al., 2017), again at the expense of increased inner working angles.

For unobstructed telescope pupils, all starlight will be blocked by both the FQPM and vortex coronagraphs. However, for obstructed pupils there will be star light leaking through. One of the solutions that has been investigated is adding an apodizer in the pupil plane upstream from the focal-plane mask. For simple circularly-symmetric pupils, analytical solutions can be derived for this apodizer (Fogarty et al., 2017; Mawet et al., 2013a), and numerical apodizers can be found for non-symmetric telescope pupils as well (Carlotti, 2013; Ruane et al., 2016).

The vortex coronagraph has seen successful deployment on many ground-based instruments (Absil et al., 2016; Mawet et al., 2013b; Serabyn et al., 2010, 2017) and is the basis for the future HabEx space telescope (Gaudi

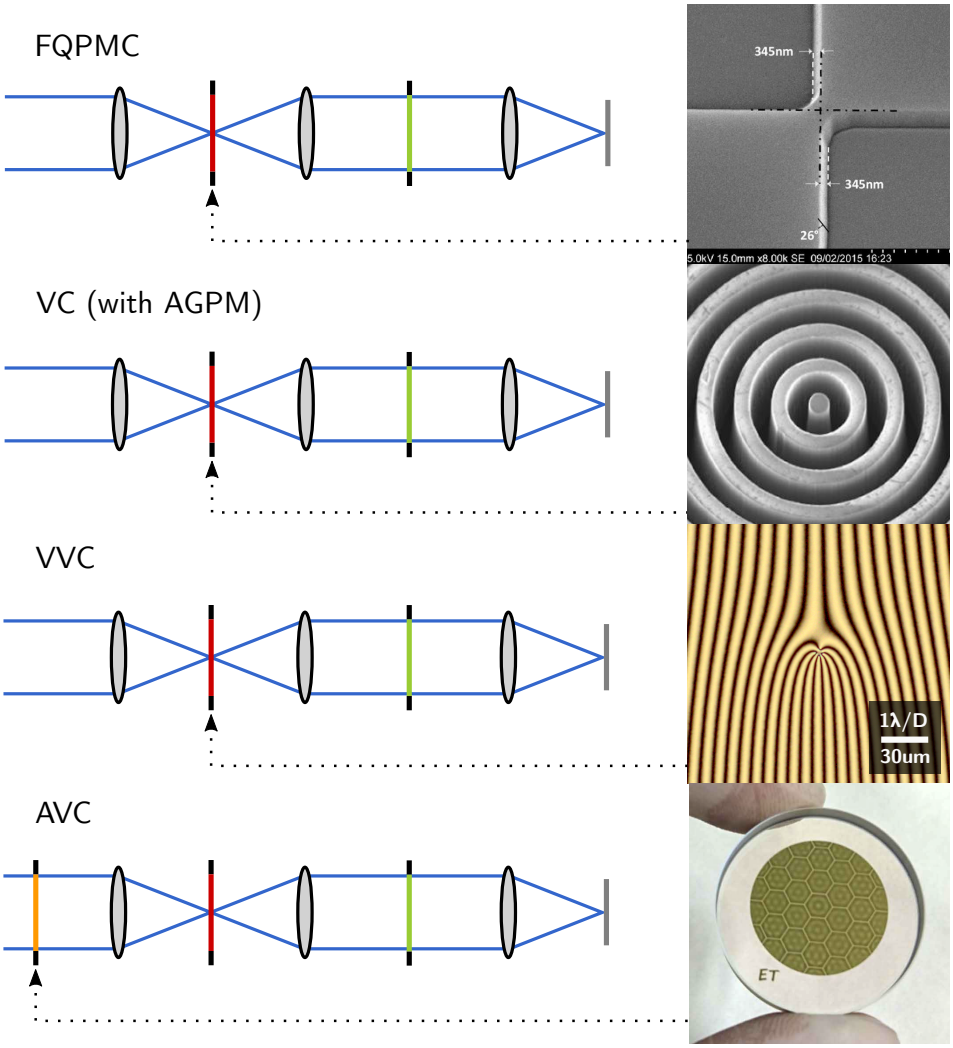

Figure 1.13: Schematic optical layouts of four types of phase-mask coronagraphs. The scanning electron microscope, optical microscope and photographic images are adapted from Bonafous et al. (2016), Delacroix et al. (2013), Doelman et al. (2020), and Llop-Sayson et al. (2020).

et al., 2020), which is an off-axis telescope built specifically to accommodate a vortex coronagraph.

Pupil-plane coronagraphs

One final category of coronagraphs are the pupil-plane coronagraphs. These do not share the same optical layout as the Lyot coronagraph, but instead consist of only a single pupil-plane apodizer and no focal-plane mask or Lyot stop. This mask is designed in such a way as to suppress the light in a region of interest around the star. As the planet PSF is the same as the stellar PSF, the mask additionally needs to maximize the amount of light in the core of the PSF to retain planet throughput. While this may seem a step back from the Lyot coronagraph, their significantly reduced optical complexity and ability to work for arbitrary telescope pupil geometries lets them see widespread adoption on current ground based telescopes, for example on Magellan/MagAO (Otten et al., 2017), Subaru/SCExAO (Doelman et al., 2017), VLT/ERIS (Boehle et al., 2018; Kenworthy et al., 2018b), LBT/LMIRcam (Doelman et al., 2020), HiCIBaS (Marchis et al., 2018), and on the future ELT instrument METIS (Kenworthy et al., 2018a).

Shaped pupil coronagraphs attempt to do the apodization by only modifying the amplitude of the light. Early apodizers were based on analytical expressions (Kasdin et al., 2003), while later global optimization methods were developed to derive the best possible apodizers (Carlotti et al., 2011). Inherent to introducing only amplitude apodization in the pupil, the region of interest necessarily has to be point-symmetric around the star. While never deployed on any major high-contrast imaging instruments, this coronagraph was instrumental to the development of the APLC described above. Additionally, it provided the coronagraph for early wavefront control experiments.

The apodizing phase plate (APP) coronagraph performs the apodization by only modifying the phase of the light. Early apodizers were designed using iterated Fourier transforms (Codona et al., 2006), while later global optimization were developed to derive the best possible apodizers (Por, 2017), described in Chapter 2 of this thesis. Phase only apodizers are now proven to always perform better than amplitude apodizers, albeit often only by a small margin. Contrary to the shaped pupil coronagraphs, the APP coronagraph can produce PSFs with a region of interest on only one side of the star, which provides a higher planet throughput at the expense of a smaller field of view. Early implementations were manufactured by using diamond turning to directly write the phase pattern of the apodizer

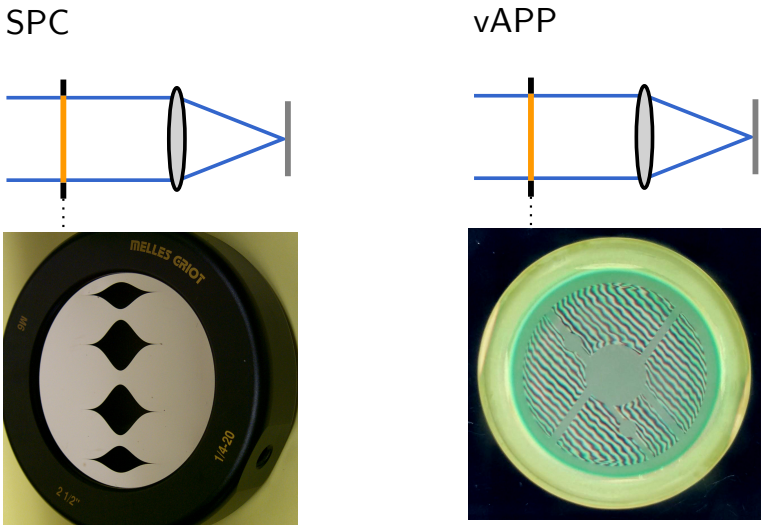

Figure 1.14: Schematic optical layouts of the two types of pupil-plane coronagraphs. The photographic images are adapted from Kasdin et al. (2004) and Doelman et al. (2017).

in a glass substrate Kenworthy et al. (2007) and discovered HD100546b (Quanz et al., 2013) and produced the first thermal light images of Beta Pictoris b (Quanz et al., 2010). The development of vectorial phase plates by Otten et al. (2017); Snik et al. (2012) made these obsolete, providing efficient achromatic phase apodization over a full photometric band.

1.3.2 The wavefront control system

The wavefront control system, or adaptive optics system as it is usually called on ground-based telescopes, corrects for any wavefront distortion in real time, whether originating from the turbulence in the atmosphere or the instrument optics (Babcock, 1953). It uses a wavefront sensor (WFS) to measure the incoming aberration, and a wavefront corrector to apply the opposite aberration, effectively flattening the wavefront. Due to the limited number of actuators on the deformable mirror – typically a few thousand on current generation devices – low spatial frequencies will be well corrected, while high spatial frequencies cannot be controlled. This results in a circular or square *control region* on the image where the PSF is well corrected, while outside this region no correction can be discerned.

The wavefront sensor typically uses shorter wavelength light split off by

a beam splitter from the longer wavelength light in the science beam, which yields a wavefront measurement that is close to, but not exactly equal to, the wavefront at the science instrument. The difference between the wavefront at the wavefront sensor and at the science instrument is called *non-common-path aberration* (NCPA). NCPAs are dynamic, and can limit the performance of the instrument when not removed well enough (Martinez et al., 2013). In addition to the fast wavefront sensor upstream, current solutions favour additional focal-plane wavefront sensing at the science instrument (Jovanovic et al., 2018) or a secondary wavefront sensor situated as close as possible to, or preferably even integrated into, the coronagraph (N'Diaye et al., 2013; Shi et al., 2018).

There are many different options for the wavefront sensor. One of the most commonly-used is the *Shack-Hartmann WFS* (SH-WFS; Hartmann 1900; Shack 1971), shown schematically in Figure 1.15. This WFS uses a microlens array in a conjugate pupil plane, creating a small image of the star for each lenslet. By measuring the shift of each spot from the on-axis position, we measure the local tilt of the wavefront at that lenslet and therefore are able to recover the wavefront in the pupil by use of an algorithmic transformation. Due to its simplicity and dynamic range, the SH-WFS has been implemented in a large number of adaptive optics systems (Beuzit et al., 2019; Lenzen et al., 2003; Macintosh et al., 2014; Rousset et al., 2003; Wizinowich et al., 2000).

Two other WFSs deserve mentioning. The *Pyramid WFS* (PyWFS; Ragazzoni 1996) uses a prism in the focal plane to split up the image into multiple (typically four) pupils. The wavefront can be reconstructed from these pupil images. The PyWFS has a much higher sensitivity, but requires sophisticated prisms (Lardière et al., 2017; Tozzi et al., 2008) and trades in dynamic range (Burvall et al., 2006; Ragazzoni, 1996). Better reconstruction algorithms seem to alleviate the latter problem at the expense of computational power (Frazin, 2018; Landman & Haffert, 2020). The PyWFS has been implemented on several HCI instruments, eg. Subaru/SCExAO (Jovanovic et al., 2015) and LBT/FLAO (Esposito et al., 2010)), and is planned to be implemented on most HCI instruments under development, eg. Magellan/MagAO-X (Males et al., 2018) and ELT/METIS (Brandl et al., 2016).

Finally, the *Zernike WFS* (Zernike, 1935) uses a phase dimple in the focal plane to produce a single pupil image in which the phase is encoded in the amplitude. This WFS has an optimal sensitivity (Guyon, 2005), but a tiny dynamic range. Amplitude aberrations need to be calibrated

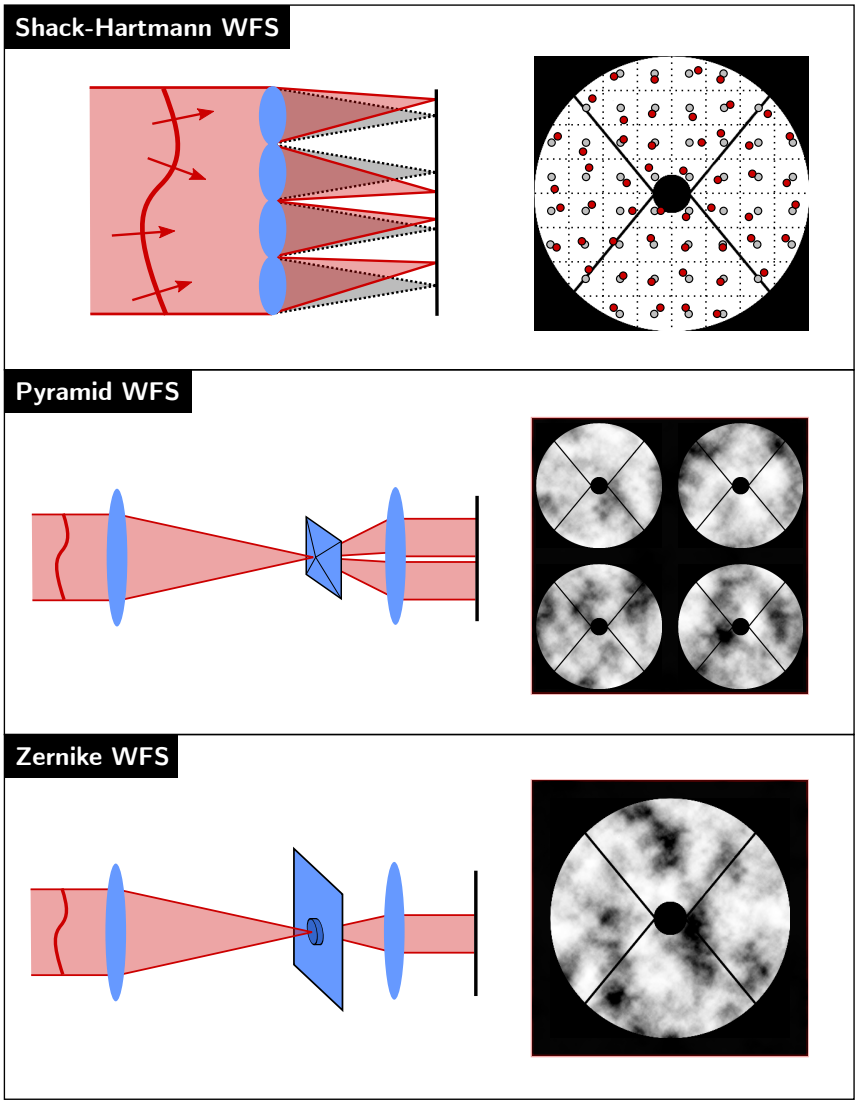

Figure 1.15: Three common wavefront sensors: the Shack-Hartmann, Pyramid and Zernike wavefront sensor. A schematic optical layout is shown on the left, and an example output for an aberrated wavefront on the right, for each of the wavefront sensors.

out, which is usually done sequentially (N'Diaye et al., 2013). Solutions to this problem have been proposed (Doelman et al., 2019), though not widely implemented as of yet. Despite these hurdles, the Zernike WFS is an attractive candidate for removing slowly-evolving aberrations, such as those due to NCPAs (N'Diaye et al., 2013; Vigan et al., 2019) or at space-based observatories (Pueyo et al., 2017).

1.3.3 Image post processing

From a photon noise perspective, separating planet light from star light should be done optically and before detection of the individual photons. However it is still possible to improve upon the raw contrast in our images with post-facto image processing methods, essentially for free provided that we observe in a manner amendable to the chosen post-processing method. The main theme in most of these methods comes back to the fact that the stellar light properties differ from the planet light properties (coherence, spectral energy distributions, position on the sky with respect to each other).

The stellar image is assumed to be stationary between images, or only vary in a limited number of degrees of freedom, presumably related to the degrees of freedom in the optical system and long-term atmospheric optical transfer function. This allows us to build a model of the stellar image without contributions from planet or disk photons, and subtract that from our observed image(s). This however requires some type of *diversity*, where the planet light behaves differently than the star light in some way.

- Reference Differential Imaging (RDI; Choquet et al. 2015; Lafrenière et al. 2009) uses a series of reference images of known single stars with similar spectral energy distributions, taken with the same instrument, to provide the stellar reference image.
- Angular Differential Imaging (ADI; Marois et al. 2006) uses the rotation of the sky, and therefore also the planet and disk, with respect to the telescope.
- Spectral Differential Imaging (SDI; Smith 1987) uses the difference in spectral signature between star and planet light.
- Polarization Differential Imaging (PDI; Kuhn et al. 2001) uses the different in polarization signature between star and planet light.

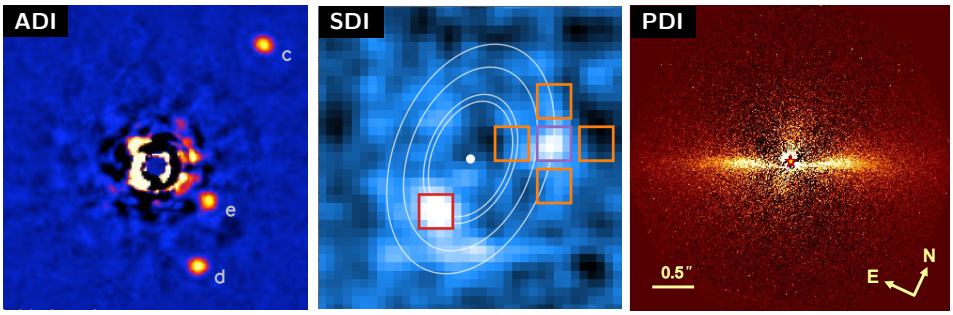

Figure 1.16: Example output images for different image post-processing techniques. (a) The discovery image of HR8799e, the fourth planet in this system using ADI (Marois et al., 2010). (b) The discovery of PDS 70c using its H-alpha emission with SDI (Haffert et al., 2019). (c) The HIP 79977 debris disk in polarized light using PDI (Engler et al., 2017).

- Coherent Differential Imaging (CDI; Guyon 2004) uses the fact that star light can interfere constructively and destructively with the stellar core, while planet and disk light can not.
- Finally, Orbital Differential Imaging (ODI; Males et al. 2015) uses the movement of the planet during its orbit over time as diversity signal.

Of course, multiple diversities can be combined to further improve the retrieved stellar reference image (eg. Christiaens et al. 2019 and Flasseur et al. 2020). In Figure 1.16, I show a few examples of images retrieved with these data processing techniques, typically gaining one or two decades in contrast on top of the raw contrast of the raw images.

1.4 This thesis

This thesis explores possible novel approaches to high-contrast imaging instruments, concerning coronagraphy, wavefront sensing and the tools that we use to study the complex interplay between these systems.

Chapter 2: optimal design of apodizing phase plate

Chapter 2 presents the development of an optimal optimization method for apodizing phase plate coronagraphs. As this optimization method can be proven to be globally optimal, that is, it will always find the best possible

solution to the problem, it supersedes previous methods that do not possess this property. I derive the fundamental limits for the APP coronagraph.

Chapter 3 & 4: the single-mode complex amplitude refinement coronagraph

Chapter 3 presents the theoretical development of the single-mode complex amplitude refinement (SCAR) coronagraph. This novel coronagraph concept consists of a pupil-plane phase plate and a microlens-fed single-mode fiber array in the focal plane. The phase plate is designed such that the contrast is achieved after the single-mode fibers instead of before, as is the convention for most coronagraphs. This additional filtering significantly improves performance, allowing us to search for exoplanets closer to the diffraction limit compared to the APP coronagraph.

Chapter 4 presents the first laboratory demonstration of the SCAR coronagraph. We demonstrate a 1×10^{-4} contrast at $1\lambda/D$ using manufactured SCAR liquid-crystal phase plates. We also perform a Monte-Carlo tolerance analysis for observing the exoplanet Proxima b using the VLT/SPHERE instrument.

Chapter 5: high-contrast imaging for Python

Chapter 5 presents the development of the software package High-Contrast Imaging for Python (HCIPy). HCIPy is an open-source modular Python package for high-contrast imaging on current and future telescopes. By integrating atmospheric simulation, wavefront sensing and coronagraphy in a single library, HCIPy enables both rapid prototyping of individual system elements and the full high-contrast imaging system.

Chapter 6: the asymmetric wind-driven halo

Chapter 6 describes an explanation for the asymmetry in the wind-driven halo observed in high-contrast imaging systems. The delay between the measurement of wavefront aberrations in the atmosphere and the correction of those aberrations with the deformable mirror in the adaptive optics system causes a butterfly-like halo to appear in high-contrast images. Interference with scintillation speckles caused by high-altitude turbulence causes one wing of the butterfly to brighten and the other to dim, making the image asymmetric.

Chapter 7 & 8: the phase-apodized-pupil Lyot coronagraph

Chapter 7 presents the theoretical development of the phase-apodized-pupil Lyot coronagraph. This novel coronagraph consists of a pupil-plane phase plate, a focal-plane mask and a Lyot stop. Using a knife-edge focal-plane mask and a one-sided dark zone, one can achieve high-throughput designs for space-based telescopes at small inner working angles. We explore the design parameters and present several designs for realistic telescope pupils.

Chapter 8 presents the first laboratory demonstration of the PAPLC on the *Très Haute Dynamique 2* (THD2) testbed at the Observatoire de Paris. It also describes and tests an integrated high-order wavefront sensor using only light reflected by the focal-plane mask. We demonstrate raw contrasts comparable to other coronagraphs on the THD2, and wavefront sensing performance comparable with the fundamental photon noise limit.

1.5 Future outlook

The wide variety of developed coronagraphs, wavefront sensors and post-processing methods is a testament to the enthusiasm of instrumentalists and the discovery of thousands of exoplanets. The first generation of high-contrast imaging instruments are currently being upgraded to use new coronagraphs and AO systems. GPI 2.0 (Chilcote et al., 2018), SPHERE+ (Boccaletti et al., 2020) and the continually refined SCExAO will be seeing more on-sky operation in the following years, both in testing and in scientific capacity. Additionally, preparations are well underway for the Roman Space Telescope, which should be the first major test of high contrast imaging from space with a wavefront control system. While only a technology demonstrator, a successful deployment and operation should pave the way towards more ambitious projects, such as HabEx, which could provide around ten spectra of an exo-Earths (Gaudi et al., 2020), or LUVOIR, which could provide several tens (The LUVOIR Team, 2019).

As always, we must take care in comparing the resulting performance characteristics between different instruments and even subsystems, for two reasons. First, performance is highly dependent on environmental conditions – seeing conditions, phenomena such as the low-wind effect (Milli et al., 2018), and vibrational or thermal environment – can significantly influence the results, and the limited time available on world-class facilities makes it hard to obtain data under comparable conditions. Secondly, the interplay between different subsystems is crucial, so comparison needs to be done at the system level, not the sub-system level, which is not trivial.

Science output, that is, exoplanet candidate yield, should be our ultimate metric, but we have not found enough to yet place useful constraints. We are limited to comparing contrast curves of sensitivity versus angular separations,and sometimes even this is condensed into a single quantity. Unless standardized, the resulting curves are meaningless by themselves and require extensive knowledge of both systems to be comparable. First attempts at standardization of contrast have been made (Marois et al., 2008; Pairet et al., 2019; Ruane et al., 2018; Ruffio et al., 2018), which highlight the complications of providing a sufficiently good quantity for comparison. Unless these are adopted by the community, we risk the pitfall of adding yet another metric to the stack.

Simulations might be the only way to fairly compare coronagraph and wavefront control systems. The current mission of the Segmented Coronagraphs Design and Analysis (SCDA) study is to link exoplanet candidate yields to aberration sensitivity, especially those for giant space-based segmented telescopes. In doing so, it is developing a standardized way of sharing coronagraph designs, and (re)formalizing the interfaces to software packages capable of calculating exoplanet candidate yields (such as AYO, described above). This effort should streamline collaboration between research groups and allow for simpler comparison between coronagraph solutions.

While SCDA will provide excellent empirical knowledge on how aberrations impact exoplanet candidate yield, it does not provide an explanatory knowledge. Belikov et al. (2019) provides an initial step for perfect coronagraphs, which will become increasingly relevant as coronagraph designs progress towards this level of perfection.

An open question is still to what degree the coronagraph, wavefront sensor and wavefront control system can help each other. One option could be for the coronagraph to extract photons for high-order wavefront sensing in a more smart way than the conventional beam splitter, without affecting the coronagraphic image; another option is to tune the wavefront control system to allow more power in modes that are better suppressed by the coronagraph. Both may be combined for further improvements.

For both ground- and space-based instruments, predictive control will be a groundbreaking advancement, as it allows for a significantly more efficient use of the available photons. By using spatial-temporal correlations instead of just spatial correlations, it can provide a controlled wavefront beyond the sensing limit of the individual wavefront sensor frames. This improves raw contrast and also, perhaps more importantly, secondary effects

such as the asymmetry in the wind-driven halo (see Chapter 6) by temporally decorrelating the residual atmospheric speckles. Predictive control requires us to consistently nail the changing spatial-temporal correlations, either using brute-force based on wavefront sensor telemetry (Guyon & Males, 2017) of even better, based on this telemetry and a system model, where the model acts as prior knowledge to reduce the number of parameters that need to be estimated in real time. Additionally, this improved modeling can help us pinpoint which parts of our instrument need to be improved. While attempted for many years, recent advances in machine learning and computational performance bring this goal closer than ever.

These technological advances will enable future ground-based telescopes, such as the ELT, GMT and TMT, to characterize rocky exoplanets around nearby lower-mass stars in the near and mid-infrared. In addition to their orbital properties, photometric monitoring campaigns will enable the determination of their rotational periods (including giant gas planets) and multi-year campaigns of rocky exoplanets may reveal the presence of seasons and continents (Robinson et al., 2011). In combination with high resolution spectroscopy, biomarker gases may be detectable in their atmospheres. Smaller-aperture space-based telescopes (e.g. the Roman Space Telescope) will search for and characterise rocky planets around solar-type stars. Looking to the next few decades, four large space telescope missions are being proposed that will have the angular resolution to image and characterize dozens of exoplanets, enabling us to maybe answer whether there is life elsewhere in the Universe.

1

References

Absil, O., Mawet, D., Karlsson, M., et al. 2016, in Society of Photo-Optical Instrumentation Engineers (SPIE) Conference Series, Vol. 9908, Ground-based and Airborne Instrumentation for Astronomy VI, 99080Q

Babcock, H. W. 1953, PASP, 65, 229

Bashi, D., Helled, R., Zucker, S., & Mordasini, C. 2017, A&A, 604, A83, doi: 10.1051/0004-6361/201629922

Bate, M. R. 1998, ApJ, 508, L95, doi: 10.1086/311719

Beichman, C., Stapelfeldt, K., Patel, R., Meshkat, T., & ygouf, m. 2018, in American Astronomical Society Meeting Abstracts, Vol. 231, American Astronomical Society Meeting Abstracts #231, 246.46

Belikov, R., Sirbu, D., Bendek, E., et al. 2019, in American Astronomical Society Meeting Abstracts, Vol. 233, American Astronomical Society Meeting Abstracts #233, 237.02

Beuzit, J. L., Vigan, A., Mouillet, D., et al. 2019, A&A, 631, A155, doi: 10.1051/0004-6361/201935251

Boccaletti, A., Chauvin, G., Mouillet, D., et al. 2020, arXiv e-prints, arXiv:2003.05714. https://arxiv.org/abs/2003.05714

Boehle, A., Glauser, A. M., Kenworthy, M. A., et al. 2018, in Society of Photo-Optical Instrumentation Engineers (SPIE) Conference Series, Vol. 10702, Ground-based and Airborne Instrumentation for Astronomy VII, 107023Y

Bonafous, M., Galicher, R., Baudoz, P., Firminy, J., & Boussaha, F. 2016, in Society of Photo-Optical Instrumentation Engineers (SPIE) Conference Series, Vol. 9912, Advances in Optical and Mechanical Technologies for Telescopes and Instrumentation II, 99126J

Borucki, W. J., Koch, D., Basri, G., et al. 2010, Science, 327, 977

Boss, A. P. 1997, Science, 276, 1836

Brandl, B. R., Agócs, T., Aitink-Kroes, G., et al. 2016, in Society of Photo-Optical Instrumentation Engineers (SPIE) Conference Series, Vol. 9908, Ground-based and Airborne Instrumentation for Astronomy VI, 990820

Burvall, A., Daly, E., Chamot, S. R., & Dainty, C. 2006, Optics Express, 14, 11925, doi: 10.1364/OE.14.011925

Carlotti, A. 2013, A&A, 551, A10, doi: 10.1051/0004-6361/201220661

Carlotti, A., Vanderbei, R., & Kasdin, N. J. 2011, Optics Express, 19, 26796, doi: 10.1364/OE.19.026796

Casertano, S., Lattanzi, M. G., Sozzetti, A., et al. 2008, A&A, 482, 699, doi: 10.1051/0004-6361:20078997

Cavarroc, C., Boccaletti, A., Baudoz, P., Fusco, T., & Rouan, D. 2006, A&A, 447, 397, doi: 10.1051/0004-6361:20053916

Chilcote, J. K., Bailey, V. P., De Rosa, R., et al. 2018, in Society of Photo-Optical Instrumentation Engineers (SPIE) Conference Series, Vol. 10702, Ground-based and Airborne Instrumentation for Astronomy VII, 1070244

Choquet, É., Pueyo, L., Soummer, R., et al. 2015, in Society of Photo-Optical

Instrumentation Engineers (SPIE) Conference Series, Vol. 9605, Techniques and Instrumentation for Detection of Exoplanets VII, 96051P

Christiaens, V., Casassus, S., Absil, O., et al. 2019, MNRAS, 486, 5819, doi: 10.1093/mnras/stz1232

Ciesla, F. J., & Cuzzi, J. N. 2006, Icarus, 181, 178, doi: 10.1016/j.icarus.2005.11.009

Claudi, R. U., Turatto, M., Gratton, R. G., et al. 2008, in Society of Photo-Optical Instrumentation Engineers (SPIE) Conference Series, Vol. 7014, Ground-based and Airborne Instrumentation for Astronomy II, 70143E

Codona, J. L., Kenworthy, M. A., Hinz, P. M., Angel, J. R. P., & Woolf, N. J. 2006, in Society of Photo-Optical Instrumentation Engineers (SPIE) Conference Series, Vol. 6269, 62691N

Dawson, R. I., & Johnson, J. A. 2018a, ARA&A, 56, 175, doi: 10.1146/annurev-astro-081817-051853

—. 2018b, ARA&A, 56, 175, doi: 10.1146/annurev-astro-081817-051853

de Boer, J., Langlois, M., van Holstein, R. G., et al. 2020, A&A, 633, A63, doi: 10.1051/0004-6361/201834989

Delacroix, C., Absil, O., Forsberg, P., et al. 2013, A&A, 553, A98, doi: 10.1051/0004-6361/201321126

Doelman, D. S., Fagginger Auer, F., Escuti, M. J., & Snik, F. 2019, Optics Letters, 44, 17, doi: 10.1364/OL.44.000017

Doelman, D. S., Por, E. H., Ruane, G., Escuti, M. J., & Snik, F. 2020, PASP, 132, 045002, doi: 10.1088/1538-3873/ab755f

Doelman, D. S., Snik, F., Warriner, N. Z., & Escuti, M. J. 2017, in Society of Photo-Optical Instrumentation Engineers (SPIE) Conference Series, Vol. 10400, Society of Photo-Optical Instrumentation Engineers (SPIE) Conference Series, 104000U

Dominik, C., Blum, J., Cuzzi, J. N., & Wurm, G. 2007, in Protostars and Planets V, ed. B. Reipurth, D. Jewitt, & K. Keil, 783

Engler, N., Schmid, H. M., Thalmann, C., et al. 2017, A&A, 607, A90, doi: 10.1051/0004-6361/201730846

Esposito, S., Riccardi, A., Fini, L., et al. 2010, in Society of Photo-Optical Instrumentation Engineers (SPIE) Conference Series, Vol. 7736, Adaptive Optics Systems II, 773609

Fischer, D. A., Anglada-Escude, G., Arriagada, P., et al. 2016, PASP, 128, 066001, doi: 10.1088/1538-3873/128/964/066001

Flasseur, O., Denis, L., Thiébaut, É., & Langlois, M. 2020, A&A, 637, A9, doi: 10.1051/0004-6361/201937239

Fogarty, K., Pueyo, L., Mazoyer, J., & N'Diaye, M. 2017, AJ, 154, 240, doi: 10.3847/1538-3881/aa9063

Foo, G., Palacios, D. M., & Swartzland er, Grover A., J. 2005, Optics Letters, 30, 3308

Frazin, R. A. 2018, Journal of the Optical Society of America A, 35, 594, doi: 10.1364/JOSAA.35.000594

Fried, D. L. 1966, Journal of the Optical Society of America (1917-1983), 56, 1372

Ftaclas, C., Siebert, E. T., & Terrile, R. J. 1988, in Space Optics for Astrophysics and Earth and Planetary Remote Sensing, Vol. 10, 62–62
Gaia Collaboration, Prusti, T., de Bruijne, J. H. J., et al. 2016, A&A, 595, A1, doi: 10.1051/0004-6361/201629272
Gaudi, B. S., Seager, S., Mennesson, B., et al. 2020, arXiv e-prints, arXiv:2001.06683. https://arxiv.org/abs/2001.06683
Greaves, J. S., Richards, A. M. S., Bains, W., et al. 2020, Nature Astronomy, doi: 10.1038/s41550-020-1174-4
Greenwood, D. P. 1977, Journal of the Optical Society of America (1917-1983), 67, 390
Guerri, G., Daban, J.-B., Robbe-Dubois, S., et al. 2011, Experimental Astronomy, 30, 59, doi: 10.1007/s10686-011-9220-y
Guyon, O. 2003, A&A, 404, 379
—. 2004, ApJ, 615, 562, doi: 10.1086/423980
—. 2005, ApJ, 629, 592, doi: 10.1086/431209
Guyon, O., & Males, J. 2017, arXiv e-prints, arXiv:1707.00570. https://arxiv.org/abs/1707.00570
Guyon, O., Martinache, F., Belikov, R., & Soummer, R. 2010, ApJS, 190, 220, doi: 10.1088/0067-0049/190/2/220
Guyon, O., Pluzhnik, E. A., Kuchner, M. J., Collins, B., & Ridgway, S. T. 2006, ApJS, 167, 81, doi: 10.1086/507630
Haffert, S. Y., Bohn, A. J., de Boer, J., et al. 2019, Nature Astronomy, 3, 749, doi: 10.1038/s41550-019-0780-5
Hartmann, J. 1900, Zeitschrift für Instrumentenkunde, 20, 47
Hinkley, S., Oppenheimer, B. R., Soummer, R., et al. 2007, ApJ, 654, 633, doi: 10.1086/509063
Hollenbach, D. J., Yorke, H. W., & Johnstone, D. 2000, in Protostars and Planets IV, ed. V. Mannings, A. P. Boss, & S. S. Russell, 401–428
Ikoma, M., Nakazawa, K., & Emori, H. 2000, ApJ, 537, 1013, doi: 10.1086/309050
Johansen, A., Klahr, H., & Henning, T. 2011, A&A, 529, A62, doi: 10.1051/0004-6361/201015979
Johansen, A., Mac Low, M.-M., Lacerda, P., & Bizzarro, M. 2015, Science Advances, 1, 1500109, doi: 10.1126/sciadv.1500109
Jovanovic, N., Martinache, F., Guyon, O., et al. 2015, PASP, 127, 890, doi: 10.1086/682989
Jovanovic, N., Absil, O., Baudoz, P., et al. 2018, in Society of Photo-Optical Instrumentation Engineers (SPIE) Conference Series, Vol. 10703, Adaptive Optics Systems VI, 107031U
Kasdin, N. J., Vanderbei, R. J., Littman, M. G., Carr, M., & Spergel, D. N. 2004, in Society of Photo-Optical Instrumentation Engineers (SPIE) Conference Series, Vol. 5487, Optical, Infrared, and Millimeter Space Telescopes, ed. J. C. Mather, 1312–1321
Kasdin, N. J., Vanderbei, R. J., Spergel, D. N., & Littman, M. G. 2003, ApJ, 582, 1147
Kenworthy, M. A., Absil, O., Carlomagno, B., et al. 2018a, in Society of

Photo-Optical Instrumentation Engineers (SPIE) Conference Series, Vol. 10702, Ground-based and Airborne Instrumentation for Astronomy VII, 10702A3

Kenworthy, M. A., Codona, J. L., Hinz, P. M., et al. 2007, ApJ, 660, 762, doi: 10.1086/513596

Kenworthy, M. A., Snik, F., Keller, C. U., et al. 2018b, in Society of Photo-Optical Instrumentation Engineers (SPIE) Conference Series, Vol. 10702, Ground-based and Airborne Instrumentation for Astronomy VII, 1070246

Knight, J. M., Guyon, O., Lozi, J., Jovanovic, N., & Males, J. R. 2018, in Society of Photo-Optical Instrumentation Engineers (SPIE) Conference Series, Vol. 10706, Advances in Optical and Mechanical Technologies for Telescopes and Instrumentation III, 107065O

Kratter, K., & Lodato, G. 2016, ARA&A, 54, 271, doi: 10.1146/annurev-astro-081915-023307

Krissansen-Totton, J., Bergsman, D. S., & Catling, D. C. 2016, Astrobiology, 16, 39, doi: 10.1089/ast.2015.1327

Kuchner, M. J., & Traub, W. A. 2002, ApJ, 570, 900, doi: 10.1086/339625

Kuhn, J. R., Potter, D., & Parise, B. 2001, ApJ, 553, L189, doi: 10.1086/320686

Lafrenière, D., Marois, C., Doyon, R., & Barman, T. 2009, The Astrophysical Journal, 694, L148, doi: 10.1088/0004-637x/694/2/l148

Landman, R., & Haffert, S. Y. 2020, Optics Express, 28, 16644, doi: 10.1364/OE.389465

Lardière, O., Pazder, J., Véran, J.-P., & van Kooten, M. 2017, Adaptive Optics for Extremely Large Telescopes V (AO4ELT5)

Larkin, J. E., Chilcote, J. K., Aliado, T., et al. 2014, in Society of Photo-Optical Instrumentation Engineers (SPIE) Conference Series, Vol. 9147, Ground-based and Airborne Instrumentation for Astronomy V, 91471K

Lenzen, R., Hartung, M., Brandner, W., et al. 2003, in Proc. SPIE, Vol. 4841, Instrument Design and Performance for Optical/Infrared Ground-based Telescopes, ed. M. Iye & A. F. M. Moorwood, 944–952

Libby-Roberts, J. E., Berta-Thompson, Z. K., Désert, J.-M., et al. 2020, AJ, 159, 57, doi: 10.3847/1538-3881/ab5d36

Llop-Sayson, J., Ruane, G., Mawet, D., et al. 2020, AJ, 159, 79, doi: 10.3847/1538-3881/ab6329

Lovis, C., Snellen, I., Mouillet, D., et al. 2017, A&A, 599, A16

Lozi, J., Martinache, F., & Guyon, O. 2009, PASP, 121, 1232, doi: 10.1086/648392

Luque, R., Nowak, G., Pallé, E., et al. 2019, A&A, 623, A114, doi: 10.1051/0004-6361/201834952

Lyot, B. 1939, MNRAS, 99, 580

Macintosh, B., Graham, J. R., Ingraham, P., et al. 2014, Proceedings of the National Academy of Science, 111, 12661

Males, J. R., Belikov, R., & Bendek, E. 2015, in Society of Photo-Optical Instrumentation Engineers (SPIE) Conference Series, Vol. 9605, Techniques and Instrumentation for Detection of Exoplanets VII, 960518

Males, J. R., Close, L. M., Miller, K., et al. 2018, in Society of Photo-Optical Instrumentation Engineers (SPIE) Conference Series, Vol. 10703, Adaptive Optics

Systems VI, 1070309
Marchis, F., Thibault, S., Côté, O., et al. 2018, in AGU Fall Meeting Abstracts, Vol. 2018, P41C–3747
Marois, C., Lafrenière, D., Doyon, R., Macintosh, B., & Nadeau, D. 2006, ApJ, 641, 556
Marois, C., Lafrenière, D., Macintosh, B., & Doyon, R. 2008, ApJ, 673, 647, doi: 10.1086/523839
Marois, C., Zuckerman, B., Konopacky, Q. M., Macintosh, B., & Barman, T. 2010, Nature, 468, 1080, doi: 10.1038/nature09684
Martinez, P., Kasper, M., Costille, A., et al. 2013, A&A, 554, A41
Matsumoto, T., & Hanawa, T. 2003, ApJ, 595, 913, doi: 10.1086/377367
Mawet, D., Pueyo, L., Carlotti, A., et al. 2013a, ApJS, 209, 7, doi: 10.1088/0067-0049/209/1/7
Mawet, D., Riaud, P., Absil, O., & Surdej, J. 2005, ApJ, 633, 1191, doi: 10.1086/462409
Mawet, D., Pueyo, L., Lawson, P., et al. 2012, in Society of Photo-Optical Instrumentation Engineers (SPIE) Conference Series, Vol. 8442, Space Telescopes and Instrumentation 2012: Optical, Infrared, and Millimeter Wave, 844204
Mawet, D., Absil, O., Delacroix, C., et al. 2013b, A&A, 552, L13, doi: 10.1051/0004-6361/201321315
Mayor, M., & Queloz, D. 1995, Nature, 378, 355
Milli, J., Banas, T., Mouillet, D., et al. 2016, in Society of Photo-Optical Instrumentation Engineers (SPIE) Conference Series, Vol. 9909, Adaptive Optics Systems V, 99094Z
Milli, J., Kasper, M., Bourget, P., et al. 2018, in Society of Photo-Optical Instrumentation Engineers (SPIE) Conference Series, Vol. 10703, Adaptive Optics Systems VI, 107032A
Moody, D. C., & Trauger, J. T. 2007, in Society of Photo-Optical Instrumentation Engineers (SPIE) Conference Series, Vol. 6693, Proc. SPIE, 66931I
Murakami, N., Uemura, R., Baba, N., et al. 2008, PASP, 120, 1112, doi: 10.1086/592285
N'Diaye, M., Dohlen, K., Fusco, T., & Paul, B. 2013, A&A, 555, A94, doi: 10.1051/0004-6361/201219797
N'Diaye, M., Soummer, R., Pueyo, L., et al. 2016, ApJ, 818, 163, doi: 10.3847/0004-637X/818/2/163
Newman, K., Conway, J., Belikov, R., & Guyon, O. 2016, PASP, 128, 055003, doi: 10.1088/1538-3873/128/963/055003
Öberg, K. I., Murray-Clay, R., & Bergin, E. A. 2011, ApJ, 743, L16, doi: 10.1088/2041-8205/743/1/L16
Otten, G. P. P. L., Snik, F., Kenworthy, M. A., et al. 2017, ApJ, 834, 175
Paardekooper, S. J., & Mellema, G. 2006, A&A, 459, L17, doi: 10.1051/0004-6361:20066304
Pairet, B., Cantalloube, F., Gomez Gonzalez, C. A., Absil, O., & Jacques, L. 2019, MNRAS, 487, 2262, doi: 10.1093/mnras/stz1350
Piro, A. L., & Vissapragada, S. 2020, AJ, 159, 131, doi: 10.3847/1538-3881/

ab7192
Por, E. H. 2017, in Society of Photo-Optical Instrumentation Engineers (SPIE) Conference Series, Vol. 10400, Proc. SPIE, 104000V
Pueyo, L., Zimmerman, N., Bolcar, M., et al. 2017, in Society of Photo-Optical Instrumentation Engineers (SPIE) Conference Series, Vol. 10398, Society of Photo-Optical Instrumentation Engineers (SPIE) Conference Series, 103980F
Quanz, S. P., Amara, A., Meyer, M. R., et al. 2013, ApJ, 766, L1, doi: 10.1088/2041-8205/766/1/L1
Quanz, S. P., Meyer, M. R., Kenworthy, M. A., et al. 2010, ApJ, 722, L49, doi: 10.1088/2041-8205/722/1/L49
Ragazzoni, R. 1996, Journal of Modern Optics, 43, 289, doi: 10.1080/09500349608232742
Rando, N., Asquier, J., Corral Van Damme, C., et al. 2018, in Society of Photo-Optical Instrumentation Engineers (SPIE) Conference Series, Vol. 10698, Space Telescopes and Instrumentation 2018: Optical, Infrared, and Millimeter Wave, 106980K
Rappaport, S., Levine, A., Chiang, E., et al. 2012, ApJ, 752, 1, doi: 10.1088/0004-637X/752/1/1
Rauer, H., Catala, C., Aerts, C., et al. 2014, Experimental Astronomy, 38, 249, doi: 10.1007/s10686-014-9383-4
Ricker, G. R., Winn, J. N., Vanderspek, R., et al. 2014, in Proc. SPIE, Vol. 9143, Space Telescopes and Instrumentation 2014: Optical, Infrared, and Millimeter Wave, 914320
Robinson, T. D., Meadows, V. S., Crisp, D., et al. 2011, Astrobiology, 11, 393, doi: 10.1089/ast.2011.0642
Roddier, F., & Roddier, C. 1997, PASP, 109, 815, doi: 10.1086/133949
Rodenhuis, M., Snik, F., van Harten, G., Hoeijmakers, J., & Keller, C. U. 2014, in Society of Photo-Optical Instrumentation Engineers (SPIE) Conference Series, Vol. 9099, Polarization: Measurement, Analysis, and Remote Sensing XI, 90990L
Rodin, A. E. 2019, Astronomy Reports, 63, 224, doi: 10.1134/S1063772919030090
Rouan, D., Riaud, P., Boccaletti, A., Clénet, Y., & Labeyrie, A. 2000, PASP, 112, 1479
Rousset, G., Lacombe, F., Puget, P., et al. 2003, in Proc. SPIE, Vol. 4839, Adaptive Optical System Technologies II, ed. P. L. Wizinowich & D. Bonaccini, 140–149
Ruane, G., Jewell, J., Mawet, D., Pueyo, L., & Shaklan, S. 2016, in Society of Photo-Optical Instrumentation Engineers (SPIE) Conference Series, Vol. 9912, Proc. SPIE, 99122L
Ruane, G., Mawet, D., Jewell, J., & Shaklan, S. 2017, in Society of Photo-Optical Instrumentation Engineers (SPIE) Conference Series, Vol. 10400, Society of Photo-Optical Instrumentation Engineers (SPIE) Conference Series, 104000J
Ruane, G., Riggs, A., Mazoyer, J., et al. 2018, in Society of Photo-Optical Instrumentation Engineers (SPIE) Conference Series, Vol. 10698, Space Telescopes and Instrumentation 2018: Optical, Infrared, and Millimeter Wave, 106982S
Ruffio, J.-B., Mawet, D., Czekala, I., et al. 2018, AJ, 156, 196, doi: 10.3847/

1538-3881/aade95
Sahlmann, J., Martín-Fleitas, J., Mora, A., et al. 2016, in Society of Photo-Optical Instrumentation Engineers (SPIE) Conference Series, Vol. 9904, Space Telescopes and Instrumentation 2016: Optical, Infrared, and Millimeter Wave, 99042E
Sahlmann, J., Mora, A., Martín-Fleitas, J. M., et al. 2018, in IAU Symposium, Vol. 330, Astrometry and Astrophysics in the Gaia Sky, ed. A. Recio-Blanco, P. de Laverny, A. G. A. Brown, & T. Prusti, 343–344
Schmid, H. M., Bazzon, A., Roelfsema, R., et al. 2018, A&A, 619, A9, doi: 10.1051/0004-6361/201833620
Schwieterman, E. W., Kiang, N. Y., Parenteau, M. N., et al. 2018, Astrobiology, 18, 663, doi: 10.1089/ast.2017.1729
Serabyn, E., Mawet, D., & Burruss, R. 2010, Nature, 464, 1018, doi: 10.1038/nature09007
Serabyn, E., Huby, E., Matthews, K., et al. 2017, AJ, 153, 43, doi: 10.3847/1538-3881/153/1/43
Shack, R. V. 1971, J. Opt. Soc. Am., 61, 656
Shakura, N. I., & Sunyaev, R. A. 1973, A&A, 500, 33
Shi, F., Seo, B.-J., Cady, E., et al. 2018, in Society of Photo-Optical Instrumentation Engineers (SPIE) Conference Series, Vol. 10698, Proc. SPIE, 106982O
Shu, F. H. 1977, ApJ, 214, 488, doi: 10.1086/155274
Sivaramakrishnan, A., Soummer, R., Oppenheimer, B. R., et al. 2010, in Society of Photo-Optical Instrumentation Engineers (SPIE) Conference Series, Vol. 7735, Ground-based and Airborne Instrumentation for Astronomy III, 773586
Smith, W. H. 1987, PASP, 99, 1344, doi: 10.1086/132124
Snik, F., Otten, G., Kenworthy, M., et al. 2012, in Society of Photo-Optical Instrumentation Engineers (SPIE) Conference Series, Vol. 8450, Modern Technologies in Space- and Ground-based Telescopes and Instrumentation II, 84500M
Soummer, R. 2005, ApJ, 618, L161
Soummer, R., Aime, C., & Falloon, P. E. 2003a, A&A, 397, 1161
Soummer, R., Dohlen, K., & Aime, C. 2003b, A&A, 403, 369, doi: 10.1051/0004-6361:20030278
Soummer, R., Brady, G. R., Brooks, K., et al. 2018, in Society of Photo-Optical Instrumentation Engineers (SPIE) Conference Series, Vol. 10698, Space Telescopes and Instrumentation 2018: Optical, Infrared, and Millimeter Wave, 106981O
Stark, C. C., Roberge, A., Mandell, A., & Robinson, T. D. 2014, ApJ, 795, 122, doi: 10.1088/0004-637X/795/2/122
Suleymanova, S. A., & Rodin, A. E. 2014, Astronomy Reports, 58, 796, doi: 10.1134/S1063772914110067
The LUVOIR Team. 2019, arXiv e-prints, arXiv:1912.06219. https://arxiv.org/abs/1912.06219
Tinyanont, S., Millar-Blanchaer, M. A., Nilsson, R., et al. 2019, PASP, 131, 025001, doi: 10.1088/1538-3873/aaef0f
Tozzi, A., Stefanini, P., Pinna, E., & Esposito, S. 2008, in Society of Photo-Optical Instrumentation Engineers (SPIE) Conference Series, Vol. 7015, Adaptive Op-

tics Systems, 701558
Trauger, J., Moody, D., Krist, J., & Gordon, B. 2016, Journal of Astronomical Telescopes, Instruments, and Systems, 2, 011013, doi: 10.1117/1.JATIS.2.1.011013
Tucker, C. J. 1979, Remote Sensing of Environment, 8, 127, doi: 10.1016/0034-4257(79)90013-0
Udry, S., & Santos, N. C. 2007, ARA&A, 45, 397, doi: 10.1146/annurev.astro.45.051806.110529
van Lieshout, R., Min, M., Dominik, C., et al. 2016, A&A, 596, A32, doi: 10.1051/0004-6361/201629250
Vigan, A., N'Diaye, M., Dohlen, K., et al. 2019, A&A, 629, A11, doi: 10.1051/0004-6361/201935889
Windmark, F., Birnstiel, T., Güttler, C., et al. 2012, A&A, 540, A73, doi: 10.1051/0004-6361/201118475
Winn, J. N., & Fabrycky, D. C. 2015, ARA&A, 53, 409, doi: 10.1146/annurev-astro-082214-122246
Wizinowich, P., Acton, D. S., Shelton, C., et al. 2000, PASP, 112, 315
Wolszczan, A. 1994, Science, 264, 538, doi: 10.1126/science.264.5158.538
Wolszczan, A., & Frail, D. A. 1992, Nature, 355, 145
Zernike, F. 1935, Tech. Phys, 16, 454
Zimmerman, N. T., Eldorado Riggs, A. J., Jeremy Kasdin, N., Carlotti, A., & Vanderbei, R. J. 2016a, Journal of Astronomical Telescopes, Instruments, and Systems, 2, 011012, doi: 10.1117/1.JATIS.2.1.011012
Zimmerman, N. T., N'Diaye, M., St. Laurent, K. E., et al. 2016b, in Society of Photo-Optical Instrumentation Engineers (SPIE) Conference Series, Vol. 9904, Space Telescopes and Instrumentation 2016: Optical, Infrared, and Millimeter Wave, 99041Y